

Transient Propagation and Scattering of Quasi-Rayleigh Waves in Plates: Quantitative comparison between Pulsed TV-Holography Measurements and FC(Gram) elastodynamic simulations

Faisal Amlani^a, Oscar P. Bruno^b, José Carlos López-Vázquez^{c,*}, Cristina Trillo^c, Ángel F. Doval^c, José L. Fernández^c, Pablo Rodríguez-Gómez^c

^a*Department of Aerospace and Mechanical Engineering, University of Southern California, Los Angeles, CA 90007 (USA)*

^b*Applied and Computational Mathematics, California Institute of Technology 217-50, Pasadena, California 91125 (USA)*

^c*Departamento de Física Aplicada, Universidade de Vigo, Escola de Enxeñaría Industrial, Rúa Maxwell, s/n, Campus Universitario, E36310 Vigo, Spain*

Abstract

We study the scattering of transient, high-frequency, narrow-band quasi-Rayleigh elastic waves by through-thickness holes in aluminum plates, in the framework of ultrasonic nondestructive testing (NDT) based on full-field optical detection. Sequences of the instantaneous two-dimensional (2-D) out-of-plane displacement scattering maps are measured with a self-developed Pulsed TV Holography (PTVH) system. The corresponding simulated sequences are obtained by means of a FC(Gram) elastodynamic solver introduced recently, which implements a full three-dimensional (3D) vector formulation of the direct linear-elasticity scattering problem. A detailed quantitative comparison between these experimental and numerical sequences, which is presented here for the first time, shows very good agreement both in the amplitude and the phase of the acoustic field in the forward, lateral and backscattering areas. It is thus suggested that the combination of the PTVH system and the FC(Gram) elastodynamic solver provides an effective ultrasonic inspection tool for plate-like structures, with a significant poten-

*Corresponding author

Email address: jclopez@uvigo.es (José Carlos López-Vázquez)

tial for ultrasonic NDT applications.

Keywords: Ultrasonic nondestructive testing, Elastic waves in plates, Pulsed TV holography, Spectral simulation, Fourier continuation, High order accuracy

Declarations of interest: none.

*Abbreviations and acronyms*¹

¹Charged Coupled Device (CCD), Courant-Friedrichs-Levy (CFL), Fast Fourier Transform (FFT), Finite Differences (FD), Finite Element Method (FEM), Fourier Continuation (FC), Initial Boundary Value Problem (IBVP), Lead Zirconate Titanate (PZT), Ordinary Differential Equation (ODE), Partial differential Equation (PDE), Pulsed TV Holography (PTVH), Region Of Interest (ROI), Singular Value Decomposition (SVD), Ultrasonic Nondestructive Testing (NDT).

1. Introduction

We study the scattering of transient, high-frequency, narrow-band quasi-Rayleigh elastic waves by through-thickness holes in aluminum plates, in the framework of ultrasonic nondestructive testing (NDT) based on full-field optical detection. Our work combines an innovative experimental pulsed TV holography (PTVH) system [1] and a state-of-the-art three-dimensional (3D) FC(Gram) numerical elastodynamic solver [2] to obtain corresponding sequences of the instantaneous out-of-plane displacements at the fully two-dimensional (2D) top surface of the plates. For the first time, a detailed quantitative comparison between these experimental and numerical sequences is presented, showing very good agreement both for the amplitude and the phase of the acoustic field in the forward, lateral and backscattering areas. It is thus suggested that the combination of the PTVH system and the FC(Gram) elastodynamic solver provides an effective ultrasonic inspection tool for plate-like structures.

As it is well-known, ultrasonic techniques are a mature and powerful tool for NDT and evaluation in industry [3] with well-known benefits (deep-penetration capability with high degree of interaction with flaws or inhomogeneities, wide temporal bandwidth, high information content,...) and a wide range of different applications, particularly, in the case of ultrasonic guided waves NDT [4, 5]. Its basic principle can be described in three basic steps: first, an adequate ultrasonic field is insonified in the part to be inspected; second, interaction with defects in the material produce scattering of the insonified field; third, some physical quantity associated with the acoustic field is measured providing information about the associated scattering phenomena.

This general scheme is implemented in classical pointwise techniques employing pulse-echo or pitch-catch configurations [3] and using excitation and detection at one or two points with contact transducers (typically PZT), which renders outputs signals with high resolution in time and frequency, but normally with low spatial information content. From this well-established classical schemes, ultrasonic NDT technology has progressed in the last decades in two main complementary directions: on the one hand, developing non-contact inspection approaches [6] (f.i. air-coupled devices [7], electromagnetic acoustic transducers [8, 9] or pointwise optical generation and probing of ultrasound [10, 11]) and, on the other hand, obtaining more spatial information content about the ultrasonic field in contact techniques (f.i.

pointwise techniques with phased array transducers to control the directivity of excited or detected waves [12] or combined with some kind of scanning in detection [13] or excitation [14] or techniques with transducers spatially distributed or scanned over the part to be inspected combined with tomographic approaches [15]).

In particular, optical probing of ultrasound with full-field techniques (f.i. interferometry [16], holographic interferometry [17, 18], speckle photography [19], shearography [20] or TV-holography [21]), are intrinsically non-contact and specially well-suited for obtaining spatial information by registering images—i.e. avoiding any type of scanning over the part to be inspected—with high lateral spatial resolution and irradiance distributions correlated with the acoustic field at a given time interval, and allow the inspection or remote or inaccessible areas maintaining the previously mentioned classical benefits of NDT with ultrasound. Within this framework, those of us at the University of Vigo have demonstrated that ultrasonic non-destructive inspection can be performed in plates using a self-developed pulsed TV-holography (PTVH) system [1, 21, 22, 23] that records the two-dimensional (2D) spatial distribution of the acoustic field corresponding to the instantaneous out-of-plane displacements over the surface of the plate. As it is characteristic of full-field optical techniques, our PTVH output has high spatial resolution with a large number of spatial samples (about 10^6), even though the number of temporal samples is low (typically lower than 128). Also, in our case, the field of view for the detected 2D scattering pattern, which can be easily adapted simply by changing the imaging optics (zooming), includes tens of ultrasonic wavelengths both in the near-field and far-field zones, which means that the corresponding scattering phenomena are in the high frequency range [24]. The short acquisition time of each snapshot provides true transient analysis capability and the total measurement time to generate a complete sequence that reproduce the time evolution of 2D spatial distribution of the acoustic field, including repetitive data acquisition and processing, is typically one or two orders of magnitude shorter than with other ultrasound pointwise probing technologies. The minimum measurable out-of-plane acoustic displacement in the current prototype is of the order of one nanometer, a modest figure compared f.i. to the typical performance of laser velocimetry but adequate enough to detect the wedge-generated guided waves employed in this study.

As in any other ultrasound-based NDT approach, to extract useful information from the 2D patterns measured with our PTVH system an additional

fourth assessment step is required, namely, processing and analysis of the output signal—leading to subsequent detection, location and characterization of any existing flaws [25]. Generally speaking, this assessment process implies, implicitly or explicitly, some kind of modelling of wave propagation and scattering [26], which is usually developed in the framework of the rigorous three-dimensional (3D) vector linear elasticity theory, in conjunction with a great variety of analytical or numerical schemes (e.g. normal mode expansion method [27], finite difference method [28], finite element method (FEM) [29], boundary element method [30], discrete point source method [31], local interaction simulation approach [32], various types of combinations or hybrid methods [33, 34], etc.). In order to avoid the high computational cost typically associated to standard 3D simulation approaches in the high frequency regime, approximate theories (i.e. plate theories [35, 36] or other even more highly simplified approximations [37]), which are valid only for a limited number of situations, but that occur often in practice, have been utilized frequently [38, 39, 40].

The computational solvers employed in this contribution are based on a novel “spectral” approach: the recently introduced Fourier-Continuation (FC) method presented in [2, 41, 42, 43]. Like regular spectral solvers [44], the FC methods represent solutions by means of Fourier series, and they therefore make it possible to dramatically reduce the problematic *dispersion errors*—which accumulate in the finite-difference or finite-element approximation of the solution over domains spanning many wavelengths. But, unlike the classical Fourier-based method, the FC approach is applicable to general domains. And, unlike the Chebyshev-based methods, the FC approach utilizes regular Cartesian grids, and it therefore does not suffer from the severe Courant-Friedrichs-Levy (CFL) constraints that stem from the point-clustering inherent in Chebyshev-based explicit solvers.

As detailed in the aforementioned references, the ability of the FC method to provide high-order, low-dispersion, spectral accuracy, for general domains, stems from two main strategies, namely, 1) decomposition of the computational domain into a number of overlapping patches (following [45]); and 2) Fourier expansion along each coordinate axis, in each one of the patches, by creation of periodic functions (the continuation functions) defined in adequately chosen domains beyond the physical patch. In view of its low dispersion, the elastic FC solver has provided improvements by factors of hundreds, or even thousands and beyond, over the computing times required by other methods, for a given accuracy, for the problem of propagation of

high-frequency elastic waves [2].

As mentioned above, this contribution compares experimental values measured by PTVH with results obtained from the aforementioned FC-based elastic-wave solver, for the problem of scattering of transient quasi-Rayleigh waves by through-thickness holes. The paper is organized as follows. Section 2 establishes the nomenclature and the theoretical formulation of the direct scattering problem within the framework of the linear elasticity. Section 3 then describes details concerning the experimental methods (for excitation of quasi-Rayleigh transient wavetrains, measurement of the displacement field by PTVH and the two-step spatio-temporal Fourier transform method for deriving the final complex displacement field) as well as the numerical implementation of the FC elastic-wave solver approach. In both cases only the essential points are included for completeness: the PTVH technique was described in detail in previous contributions (see references 1, 21, 22 and 46), while a detailed description of the FC(Gram) elastic solver was presented in [2]. The experimental and simulated maps are presented in section 4, including comparisons over various specific areas in the 2-D image of the acoustic field, and the agreement between theory and experiment is discussed taking into account the pixel-wise matching of the spatial field distribution, the profiles of amplitude and phase, and the corresponding values of the global (root-mean-square) relative errors. To the best of our knowledge this is the first time that such a quantitative comparison is reported for transient waves both in near- and far-field zones, apart from our corresponding recent studies in which this work is based [2, 47]. A full 3D sequence generated by the FC(Gram) solver, displaying the temporal and spatial variation of all three components of the displacement vector both in the interior and the lateral boundaries of the plate, is also included in this section—providing useful insights on rarely observed mechanisms concerning elastic scattering. Section 5, finally, present our closing remarks.

2. Theoretical framework

We assume that for modelling wave propagation and scattering in our case it is adequate to describe plates as linear isotropic solids in the framework of linear elasticity theory within small displacement regime and linear stress-strain relationship [48, 49]. In this context, first in subsection 2.1 we introduce the notation and establish the basic equations that define the initial boundary value problem (IBVP) to be solved for the scattering of waves

in plates with stress-free boundaries in transient regime. After that, in subsection 2.2 we consider the particular properties that can be used in the case of the scattering of quasi-Rayleigh wavetrains.

2.1. Formulation of the direct scattering problem

Using the Cartesian reference frame of figure 1, with origin at point O_x and orthonormal base vectors \mathbf{a}_1 , \mathbf{a}_2 and \mathbf{a}_3 , the position of a material point of the plate P in the reference configuration is characterized by its Cartesian coordinates (x_1, x_2, x_3) which are the components of its position vector $\mathbf{x} = x_1\mathbf{a}_1 + x_2\mathbf{a}_2 + x_3\mathbf{a}_3$ (for the sake of brevity we simply write $\mathbf{x} = (x_1, x_2, x_3)$). When a wave perturbation propagates in the plate, the associated movement of P with respect to its reference position \mathbf{x} at a given time instant t is specified by the displacement field

$$\mathbf{u}(\mathbf{x}, t) = \sum_{i=1}^3 u_i(\mathbf{x}, t) \mathbf{a}_i \quad (1)$$

with components that can always be written as

$$u_i(\mathbf{x}, t) = u_{im}(\mathbf{x}, t) \cos[\varphi_{im}(\mathbf{x}, t) - 2\pi ft], \quad i = 1, 2, 3 \quad (2)$$

where $u_{im}(\mathbf{x}, t)$ and $\varphi_{im}(\mathbf{x}, t)$ are the acoustic amplitude and the acoustic phase, respectively ($\varphi_{iM}(\mathbf{x}, t) = \varphi_{im}(\mathbf{x}, t) - 2\pi ft$ is referred as the total acoustic phase). Despite the fact expression (2) is formally valid in general, it is particularly useful in two important particular cases: on the one hand, for perturbations with harmonic time-dependence at a given temporal frequency f with displacement field $\mathbf{u}_f(\mathbf{x}, t)$ and harmonic components $u_{if}(\mathbf{x}, t)$, because in this case the associated acoustic amplitudes $u_{ifm}(\mathbf{x})$ and acoustic phases $\varphi_{ifm}(\mathbf{x})$ are truly time-independent fields; on the other hand, for transient narrow-band perturbations with a central temporal frequency f_R , as those employed in our experiments, because the associated acoustic amplitudes and acoustic phases are nearly constant within any time interval of the order of the central period of the wavetrain $T_R = 1/f_R$ in such a way that they can be understood in close analogy with the harmonic case, except perhaps in areas that are in the leading and trailing edges of the wavetrain (see figure 2).

Considering that the wave perturbation can be described using the small strain regime, we have an associated strain tensor $\boldsymbol{\epsilon}(\mathbf{x}, t)$ with components

$$\epsilon_{ij}(\mathbf{x}, t) = \frac{1}{2} \left[\frac{\partial u_i(\mathbf{x}, t)}{\partial x_j} + \frac{\partial u_j(\mathbf{x}, t)}{\partial x_i} \right], \quad i, j = 1, 2, 3 \quad (3)$$

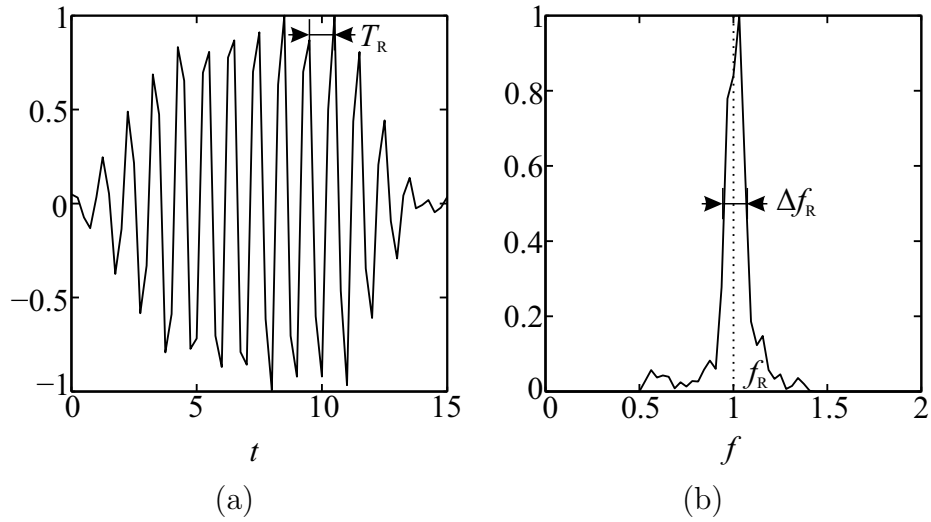


Figure 2: (a) Typical temporal record of the out-of-plane component of the incident field $u_3^i(\mathbf{x}_h, t)$ at a given point over the top surface of the plate \mathbf{x}_h for a narrow-band quasi-Rayleigh wavetrain with central excitation frequency $f_R = 1.00$ MHz and bandwidth $\Delta f_R \ll f_R$ ($T_R = 1/f_R$), (b) amplitude of the temporal spectrum of the profile $u_3^i(\mathbf{x}_h, t)$ in (a). In both cases we show the normalized profiles as a function of t in μs and f in MHz, respectively.

are solutions of equation (5) can be decomposed in longitudinal (L) and transversal (T) wave components that propagate, respectively, with phase velocities

$$c_L = \sqrt{(\lambda_e + 2\mu_e)/\rho} \quad \text{and} \quad c_T = \sqrt{\mu_e/\rho}. \quad (6)$$

Using (6) we get $(\lambda_e + \mu_e)/\rho = (c_L^2 - c_T^2)$ and $\mu_e/\rho = c_T^2$ in such a way that we can express the constants of the Lamé-Navier equations exclusively in terms of the phase velocities.

Any solution of the Lamé-Navier equation in plates with stress-free boundaries (as it is our case) has to verify over its top side Γ_+ , its bottom side Γ_- and the hole border Γ_d the stress-free boundary condition

$$\sum_{j=1}^3 \tau_{ij}(\mathbf{x}, t) n_j(\mathbf{x}) = 0, \quad i = 1, 2, 3 \quad \mathbf{x} \in \partial\Omega \quad (7)$$

being $\partial\Omega = \Gamma_+ \cup \Gamma_- \cup \Gamma_d$ and $n_j(\mathbf{x})$ the components of the normal unit vector $\mathbf{n}(\mathbf{x})$ at point $\mathbf{x} \in \partial\Omega$ pointing outwards the plate interior Ω . Equations (5-7), with additional initial conditions for displacement and velocity in the plate interior volume Ω , are the essential elements that define the initial boundary value problem (IBVP) to be solved for the scattering of waves in plates with stress-free boundaries in the transient case.

2.2. Scattering of quasi-Rayleigh waves by through-thickness holes

In the following we circumscribe the analysis to the particular case of propagation and scattering of narrow-band quasi-Rayleigh wavetrains by through-thickness holes, with residual depth $e = 0$ (figure 1) considering how to obtain the incident field inside the plate from the value of the out-of-plane component of the incident field at the top surface of the plate. More specifically, we use the complex representation of the displacement field (see Appendix A) to present the strategy to reconstruct the complex Cartesian components of the displacement of the incident field $\hat{u}_i^i(\mathbf{x}, t)$ at any point $\mathbf{x} = (x_1, x_2, x_3)$ inside the plate from the value of the complex out-of-plane component of the displacement $\hat{u}_3^i(\mathbf{x}_h, t)$ at the corresponding point $\mathbf{x}_h = (x_1, x_2, h)$ at the top surface of the plate, which is a quantity that can be measured by our PTVH system (see figure 2.a and subsection 3.1).

Quasi-Rayleigh waves result from particular combinations of Lamb modes in the so-called quasi-Rayleigh region of the Lamb spectrum where the associated branches of the S0 and A0 modes nearly overlap (see qR region with

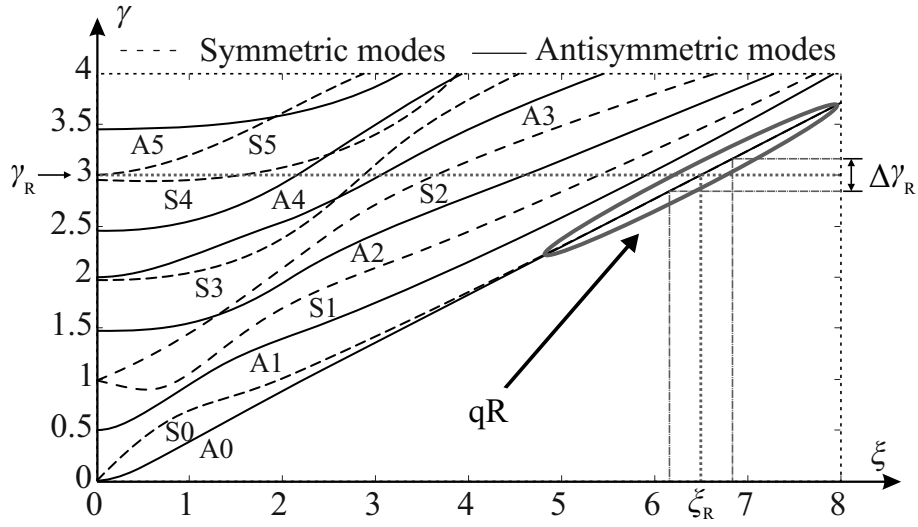


Figure 3: Frequency spectrum of Lamb propagating modes for an aluminum plate with stress-free boundaries and Poisson's ratio $\nu = 0.33$. $\gamma = 4hf/c_L$ and $\xi = 2hk/\pi$ are the normalized frequency and wavenumber respectively being c_L the longitudinal wave velocity. The location of normalized central excitation frequency $\gamma_R = 4hf_R/c_L$, normalized wavenumber $\xi_R = 4h/\lambda_R$ and normalized value of the temporal bandwidth of the pulse $\Delta\gamma_R = 4h\Delta f_R/c_L$ in our case (see section 4) are schematically represented. The branches that cross the horizontal line at γ_R correspond to the propagating Lamb modes that could be excited at the corresponding normalized temporal frequency. qR identifies the region of the spectrum that corresponds to quasi-Rayleigh waves.

$\gamma \geq 1.5$ in figure 3). A quasi-Rayleigh harmonic guided wave is just the superposition of a symmetric S0 Lamb mode and an anti-symmetric A0 Lamb mode with the same temporal frequency within the qR range and with the same value of their amplitudes at the top surface of the plate. In this conditions, the harmonic A0 and S0 modes have practically the same propagating wavenumber and a common phase velocity c_R (characterized by the common slope of the branches in the qR region) which is the Rayleigh phase velocity of the plate material. The Rayleigh equation

$$\chi_{RT}^6 - 8\chi_{RT}^4 + 8(3 - 2\chi_{TL}^2)\chi_{RT}^2 - 16(1 - \chi_{TL}^2) = 0, \quad (8)$$

where $\chi_{RT} = c_R/c_T$ and $\chi_{TL} = c_T/c_L$, shows that c_R can be obtained as a function of the longitudinal and transversal phase velocities c_L and c_T , i.e. that only two of the three phase velocities c_R , c_L and c_T are independent. If only harmonic quasi-Rayleigh waves of this type are efficiently excited by the ultrasonic source, the complex components of the complex displacement of the quasi-Rayleigh incident wavetrain (figure 2.a) can be written as the linear superposition

$$\hat{u}_i^i(\mathbf{x}, t) = \int_0^\infty w(f) \hat{u}_{if}^i(\mathbf{x}, t) df \quad i = 1, 2, 3 \quad (9)$$

where each quasi-Rayleigh harmonic complex component of frequency f can be decomposed as

$$\hat{u}_{if}^i(\mathbf{x}, t) = \hat{u}_{if}^{iS0}(\mathbf{x}, t) + \hat{u}_{if}^{iA0}(\mathbf{x}, t) \quad i = 1, 2, 3 \quad (10)$$

being $\hat{u}_{if}^{iS0}(\mathbf{x}, t)$ and $\hat{u}_{if}^{iA0}(\mathbf{x}, t)$, respectively, the corresponding harmonic complex components of the S0 and A0 modes with temporal frequency f and $w(f)$ a scalar function that specifies the weight of each harmonic quasi-Rayleigh displacement of frequency f within the qR range spectrum of the quasi-Rayleigh pulse. We will assume that $w(f)$ is peaked around a temporal frequency f_R and takes non zero values over a bandwidth interval $\Delta f_R \ll f_R$ (figure 2.b), in such a way that each harmonic component of the pulse has a wavenumber that is very close to the central wavenumber of the train $k_R = 2\pi f_R/c_R$ within the quasi-Rayleigh region qR of the Lamb spectrum (in our experiments we employ an excitation with a normalized central temporal frequency and central wavenumber of the order of 3 and 6 respectively -see below subsection 4 and figure 3). Provided that in the scattering problem

the hole is located in the far-field region of the source it is justified, on the one hand, to assume that the phase and the amplitude of the incident field can be described as a quasi-cylindrical inhomogeneous wave that diverges from a line-source, parallel to the x_3 axis (which intersect the top surface of the plate at point F with position vector $\mathbf{x}_h^F = (x_1^F, x_2^F, h)$, see figure 1.b) and, on the other hand, to neglect the contributions of non-propagating modes in such a way that expressions (9-10) give an adequate description of the components of the displacement for the a transient narrow-band quasi-Rayleigh incident field. In addition, as the normalized transversal distribution of the complex components of the displacement field of each harmonic quasi-Rayleigh contribution is a function only of its wavenumber and the thickness of the plate we can also assume, in a first approximation, that all the harmonic quasi-Rayleigh components of the pulse share the same normalized transversal distribution for their displacements (see Appendix B). In these conditions, the value of the complex components of the complex displacement of the quasi-Rayleigh wavetrain inside the volume of the plate can be written as

$$\hat{u}_i^i(\mathbf{x}, t) = [\hat{u}_{\parallel f_{\text{Rm}}}^{\text{S0}}(x_3) + \hat{u}_{\parallel f_{\text{Rm}}}^{\text{A0}}(x_3)] \times \left[\frac{\mathbf{x}_h - \mathbf{x}_h^F}{|\mathbf{x}_h - \mathbf{x}_h^F|} \cdot \mathbf{a}_i \right] \hat{u}_3^i(\mathbf{x}_h, t) \quad i = 1, 2 \quad (11a)$$

$$\hat{u}_3^i(\mathbf{x}, t) = [\hat{u}_{\perp f_{\text{Rm}}}^{\text{S0}}(x_3) + \hat{u}_{\perp f_{\text{Rm}}}^{\text{A0}}(x_3)] \hat{u}_3^i(\mathbf{x}_h, t) \quad (11b)$$

in terms of the complex out-of-plane component $\hat{u}_3^i(\mathbf{x}_h, t)$, being $\hat{u}_{\parallel f_{\text{Rm}}}^{\text{S0}}(x_3)$ and $\hat{u}_{\perp f_{\text{Rm}}}^{\text{S0}}(x_3)$ the normalized transversal distributions of the complex amplitude of the in-plane and out-of-plane components of the S0 mode with frequency f_{R} and wavenumber k_{R} and $\hat{u}_{\parallel f_{\text{Rm}}}^{\text{A0}}(x_3)$ and $\hat{u}_{\perp f_{\text{Rm}}}^{\text{A0}}(x_3)$ the corresponding transversal distributions for the A0 mode. Extracting the real part of the result of expression (11) we finally obtain the Cartesian components of the displacement of the incident field $u_i^i(\mathbf{x}, t)$ at any point $\mathbf{x} = (x_1, x_2, x_3)$ inside the plate.

3. Materials and methods

In the following, we first describe the experimental set-up employed to generate and to detect quasi-Rayleigh wavetrains in plates (subsection 3.1), then we outline the foundations of the new FC(Gram) numerical method (subsection 3.2) and finally we present the discrete formulation of the direct

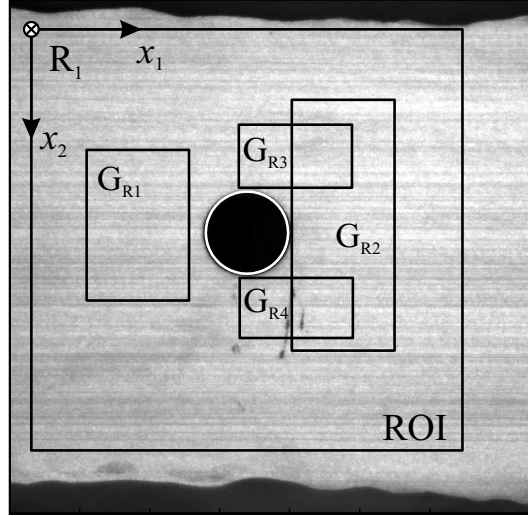


Figure 4: Reference image for a through-thickness hole ($e = 0$) of diameter $D = 12$ mm showing the region of interest (ROI) employed in the images and profiles of numerical and experimental ultrasonic fields over the plane (x_1, x_2, h) and the subzones of the ROI G_{R1}, G_{R2}, G_{R3} and G_{R4} used for quantitative assessment of the relative global error between theory and experiment (see section 4).

scattering problem (subsection 3.3) and the procedure employed for obtaining an analytic approximation to the incident field (subsection 3.4).

3.1. Experimental methods

Several through-thickness holes, with nominal diameters D in the range 4 mm to 12 mm, have been adequately prepared in aluminum plates with nominal thickness $2h = 10$ mm. In all of the cases the plates have been supported so that the constraints at their surface are minimized and plasticine has been used as acoustic absorber at the edges of the plates to minimize reflections of the incident and scattered waves that could disturb the measured acoustic fields inside the region of interest (ROI) (figure 4). The average thickness of the plates and the average diameter of the holes have been determined experimentally with a relative error lower than 1% by averaging several direct measurements obtained with a caliper with resolution of 0.05 mm and a metallographic microscope with a translation stage with resolution of 0.01 mm. The longitudinal wave velocity in the plates has been measured by means of the classical pulse-echo method resulting $c_L = 6360 (1 \pm 0.5\%)$ m/s.

The experimental system used to generate and to detect the elastic waves

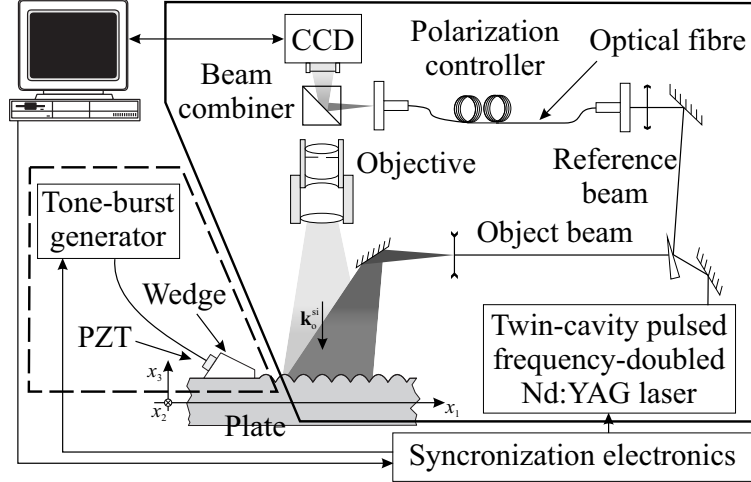


Figure 5: Experimental setup

in this plates is schematically represented in figure 5. Quasi-Rayleigh transient wavetrains have been generated by means of the classical wedge method using a short tone-burst with central frequency $f_R = 1.00$ MHz and an integer number of cycles (between 5 and 10). The instantaneous out-of-plane acoustic field at the top surface of the plate $u_3^e(\mathbf{x}_h, t)$ associated to the wavetrain during propagation and scattering has been measured with our self-developed double-pulsed TV holography system [21]. As is common in TV holography techniques [50] we employ an image-hologram configuration, sensitive to the out-of-plane component of the displacement of the surface points, with the image sensor of a video camera as recording medium. There is not optical reconstruction of the recorded holograms but instead their intensity distribution is electronically processed to render the optical phase-difference map, which depends on the displacements of the specimen surface. A twin-cavity pulsed, injection seeded and frequency doubled Nd:YAG laser (Spectron SL404T), the core of the TV holography system, emits two laser pulses, with a duration of 20 ns and a adjustable temporal inter-pulse delay τ , that are employed to record two correlograms in separate frames of a CCD camera (PCO Sensicam Double-Shutter). Each correlogram corresponds to the interference of the reference beam and the object beam scattered back by the plate surface. A processing procedure based on the spatial Fourier transform method has been applied to the correlograms [22], which renders

the so-called optical phase-change map

$$\Delta\Phi^e(\mathbf{x}_h, t) = \frac{8\pi}{\lambda_o} u_3^e(\mathbf{x}_h, t) \quad \mathbf{x}_h \in \Gamma_+ \quad (12)$$

proportional to the instantaneous out-of-plane acoustic displacement field $u_3^e(\mathbf{x}_h, t)$ being $\lambda_o = 532$ nm the wavelength of the laser and t the instant of emission of the first laser pulse. The usual scaling factor ($4\pi/\lambda_o$) between optical phase-change and displacement is doubled in equation (12) by selecting $\tau = 1.5 \mu\text{s}$ (3/2 of the period T_R associated to central excitation frequency $f_R = 1.00$ MHz, that is the minimum number of odd half-periods for which the camera can record the two correlograms in different frames).

With this scheme we have performed measurements in successive instants of the wavetrain propagation ($t_0, t_1, \dots, t_n, \dots, t_{N_o-1}$ with $t_{n+1} - t_n = \Delta t$) to obtain a complete sequence of N_o optical phase-change maps $\Delta\Phi^e(\mathbf{x}_h, t_n)$ (we have selected $N_o = 128$ with $\Delta t = 250$ ns, i.e., a quarter of the period associated to the central excitation frequency of the wavetrain). Even though this sequence of maps represents by itself a useful means to assess the interaction of the quasi-Rayleigh wavetrain and the defect for every time instant, it has been processed as a whole employing the spatio-temporal 3D Fourier transform method [46] to obtain a sequence of N_o experimental complex displacement fields $\hat{u}_3^e(\mathbf{x}_h, t_n)$, from which the acoustic amplitude $u_{3m}^e(\mathbf{x}_h, t_n) := |\hat{u}_3^e(\mathbf{x}_h, t_n)|$ and the total acoustic phase $\varphi_{3M}^e(\mathbf{x}_h, t_n) := \arg[\hat{u}_3^e(\mathbf{x}_h, t_n)]$ can be retrieved independently and a reconstructed out-of-plane displacement $u_3^e(\mathbf{x}_h, t_n) = \text{Re}[\hat{u}_3^e(\mathbf{x}_h, t_n)]$ is obtained with an improved signal-to-noise ratio. The sequence of N_o complex displacement fields $\hat{u}_3^e(\mathbf{x}_h, t_n)$ is the raw experimental data set for the comparison with numerical simulations and it is used for obtaining an analytic approximation to the incident complex field (see subsection 3.3), which is employed to define a non-homogeneous Dirichlet boundary condition in the discrete formulation of the direct scattering problem that is introduced in the following.

3.2. Numerical Method

In view of their simplicity and versatility, classical differentiation methods such as those based on use of finite differences (FD) or finite elements are often used as part of partial differential equation (PDE) discretization schemes. When applied to differential equations governing wave-like phenomena, however, approaches of this type do give rise to high numerical dispersion: phase errors accumulate over subsequent periods of a wave field, and thus FD and

FEM solvers require increasing numbers of discretization points per wavelength to resolve the solution within a given accuracy tolerance as the size of the problem grows. As is well known, methods based on use of Fourier series do not suffer from this problem: a fixed number of discretization points per wavelength suffices for such methods to produce wave-like solutions with a fixed accuracy in arbitrarily large domains (i.e. domains that can contain an arbitrarily large number of wave periods).

Unfortunately, however, classical Fourier methods are only applicable to periodic functions—since Fourier expansion of a non-periodic functions gives rise to the well-known “ringing effect” (the Gibb’s phenomenon [51]): the jump that results in the periodic extension of an inherently non-periodic function leads to an “overshoot” in the Fourier representation at points of discontinuity of the periodic continuation of the given function. This inaccuracy does not subside as more terms are added and, in fact, it results in extremely slow pointwise convergence throughout the interior of the computational domain—in addition to the unmitigated error at domain boundaries.

A goal to extend the applicability of Fourier methods (together with its inherent excellent qualities, most notably dispersionless-ness and high-order accuracy) to general non-periodic configurations has lead to the development of the FC methods that form the basis of the numerical solvers utilized in this work. The Fourier continuation (FC) method produces a rapidly-convergent interpolating Fourier series representation of a given function on a region larger than the given physical domain. This is accomplished by relying on a “periodic extension” of the given function, that closely approximates the given function values in the original domain, but which is periodic (albeit in a slightly enlarged domain) and thus suitable for Fourier approximation. The procedure is illustrated in figure 6. In detail, given a function f which is defined, without loss of generality, on the unit interval as

$$f(x) : [0, 1] \subset \mathbb{R} \rightarrow \mathbb{R},$$

the FC method produces a periodic function f^c defined on an extended interval,

$$f^c(x) : [0, b] \subset \mathbb{R} \rightarrow \mathbb{R}, \quad b > 1$$

which closely approximates $f(x)$ on the original interval $[0, 1]$.

The proposed fully-discrete Fourier continuation algorithms proceed as follows: letting N be the number of discretization points over the unit interval (yielding a uniform grid $x_i = ih, i = 0, \dots, N - 1, h = 1/(N - 1)$) together

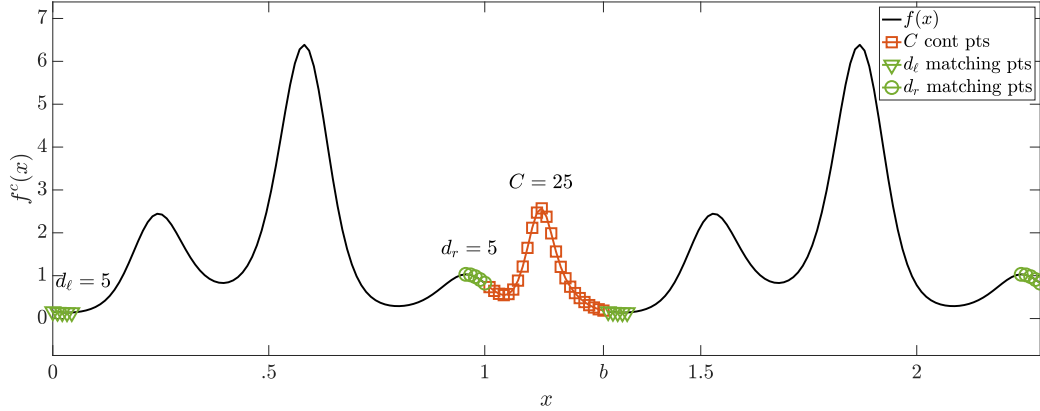


Figure 6: Fourier continuation of the non-periodic function given by $f(x) = \exp[\sin(5.4\pi x - 2.7\pi) - \cos(2\pi x)]$. Triangles/circles and squares represent $d_\ell = d_r = 5$ matching points and $C = 25$ continuation points, respectively.

with point values $f(x_i)$ of the function of interest, the Fourier continuation method produces a b -periodic trigonometric polynomial f^c of the form

$$f^c(x) = \sum_{k=-M}^M a_k \exp\left(j \frac{2\pi k x}{b}\right), \quad (13)$$

that matches the given discrete values of f : $f^c(x_i) = f(x_i)$, $i = 0, \dots, N - 1$, and which, for smooth functions f , rapidly approaches f as the N grows. Derivatives of the function can then be easily and accurately be computed through term-by-term differentiation, e.g.

$$\begin{aligned} f_x(x) &= f_x^c(x) = \sum_{k=-M}^M \left(j \frac{2\pi k}{b}\right) a_k \exp\left(j \frac{2\pi k x}{b}\right), \\ f_{xx}(x) &= f_{xx}^c(x) = - \sum_{k=-M}^M \left(\frac{2\pi k^2}{b^2}\right) a_k \exp\left(j \frac{2\pi k x}{b}\right), \quad \text{etc.} \end{aligned} \quad (14)$$

In the simplest treatment [52, 53, 54], the coefficients a_k of (13) are found by invoking the Singular Value Decomposition (SVD) to solve the least squares system

$$\min_{a_k} \sum_{i=0}^{N-1} |f^c(x_i) - f(x_i)|. \quad (15)$$

Although straightforward, repeated applications of the SVD for time-dependent function values on each line of a three-dimensional mesh in a PDE is, in general, unacceptably costly. To circumvent this difficulty, an FFT accelerated method [41, 55, 42] can be used. Relying on numbers of d_ℓ and d_r of function values nearest to the left and right endpoints of the interval (e.g. $d_\ell = d_r = 5$), the accelerated FC approach proceeds by projecting the known near-endpoint sets of function values onto certain basis of Gram discretely orthogonal polynomials. Each one of these orthogonal polynomials possesses a discrete continuation, and, thus, the near boundary values, which are given by certain linear combinations of the orthogonal-polynomial basis, can easily be continued as well. Once discrete periodic continuation functions have been determined, the corresponding Fourier coefficients can be obtained via an application of the FFT. The overall FC approximation procedure is demonstrated in Figure 6.

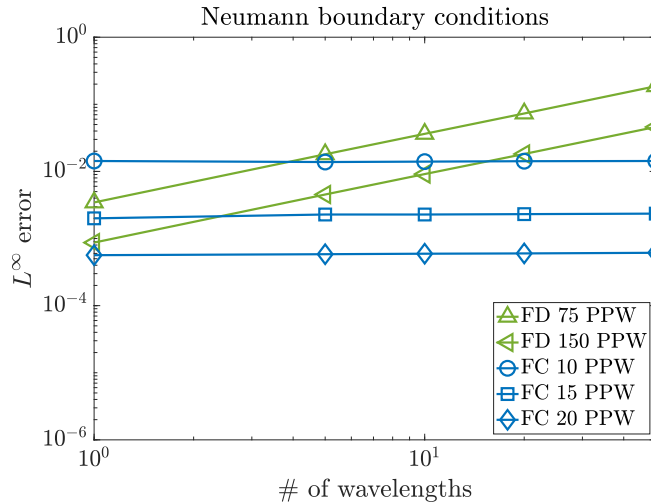


Figure 7: Plate-propagation test. Maximum numerical errors over all space and over one full temporal cycle (defined as the time required for any one crest to travel the length of the plate) are presented for a plane wave solution with increasing number of wavelengths for the 3D elastic wave equation with Neumann boundary conditions.

Using the FC method to evaluate function values and their derivatives, a time-domain PDE solver can be completed simply by incorporating an adequate ordinary differential equation (ODE) solver. Following [2] we utilize the fourth-order Adams-Bashforth (AB4) algorithm to effect the timestepping. The errors produced by the FC procedure for a simple rectangular

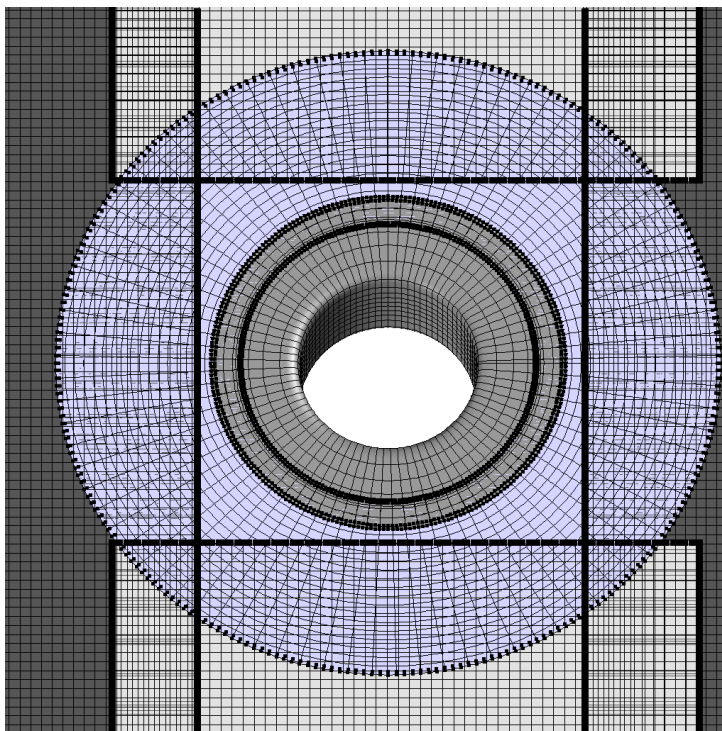


Figure 8: Close up of computational model, composed of six overlapping patches, for a through-hole on an elastic plate.

plate are illustrated in figure 7. For comparison errors resulting from use of a finite-difference method of second order are also included. The figure shows that the FC errors remain constant as the number of wavelengths increase, while the FD errors grow—in a classical manifestation of the dispersion error. Note that, additionally, even for an acoustically small plate (one wavelength along the length of the plate) a total of 150 FD discretization points per wavelength are necessary to achieve an error comparable to that resulting from the FC approach on the basis of only 20 FC points. Other comparisons in the figure provide more details in these regards. For a given accuracy tolerance, the reduced FC meshes lead to substantially reduced computing times in comparison with those required by the FD method. Figure 8 illustrates the overlapping-patch geometrical description used in conjunction with the FC approach. Full details concerning accuracy, geometry treatment and time-stepping methods used can be found in [2].

3.3. Computational specification of the experimental configuration

A discrete version of the IVBP problem specified by equations (5-7) has been developed in a prismatic computational domain with interior volume G (figure 9) using a self-developed high-precision MATLAB pre-computation for the FC(Gram) basis and a self-developed C/C++ implementation of the full 3D FC(Gram)-based elasticity solver described in subsection 3.2. Lamé-Navier equation (5-6) has been employed in G and stress-free boundary condition (7) has been applied over the top and bottom sides of the prismatic domain (which correspond to a portion of the top Γ_+ and bottom Γ_- surfaces of the plate) and over the cylindrical boundary I_1 (which corresponds to the hole border Γ_d). On top of that, the Dirichlet boundary conditions

$$u_i(\mathbf{x}^{E1}, t) = u_i^{ai}(\mathbf{x}^{E1}, t) \quad i = 1, 2, 3 \quad \mathbf{x}^{E1} \in E1 \quad (16a)$$

$$u_i(\mathbf{x}^{E2}, t) = 0 \quad i = 1, 2, 3 \quad \mathbf{x}^{E2} \in E2, \quad (16b)$$

have been imposed over the lateral exterior boundary of G , non homogeneous ones for introducing the incident field at $E1$ and homogeneous ones in the remaining part $E2$. The thickness of the computational domain has been set equal to the nominal thickness of the plates ($2h = 10$ mm). The height and the width of the top and bottom sides of the computational domain have been adequately selected in order to avoid interference in the ROI region between direct scattering phenomena and waves reflected by the exterior boundary. Null initial conditions

$$u_i(\mathbf{x}, 0) = 0 \quad i = 1, 2, 3 \quad \mathbf{x} \in G \quad (17a)$$

$$\frac{\partial u_i}{\partial t}(\mathbf{x}, 0) = 0 \quad i = 1, 2, 3 \quad \mathbf{x} \in G \quad (17b)$$

have been assumed for both displacement and velocity in G .

3.4. Analytic approximation to the incident field

For specifying the analytic approximation $u_i^{ai}(\mathbf{x}^{E1}, t)$ to the Cartesian components of the incident field used in the non-homogeneous Dirichlet boundary condition at $E1$, where $\mathbf{x}^{E1} = (0, x_2, x_3)$, we use a two-stage procedure: first, we obtain a complex analytic approximation $\hat{u}_3^{ai}(\mathbf{x}_h^{E1}, t)$ to the experimental measured out-of-plane complex component of the incident field at the top surface of the plate at $E1$, where $\mathbf{x}_h^{E1} = (0, x_2, h)$. Then, from this

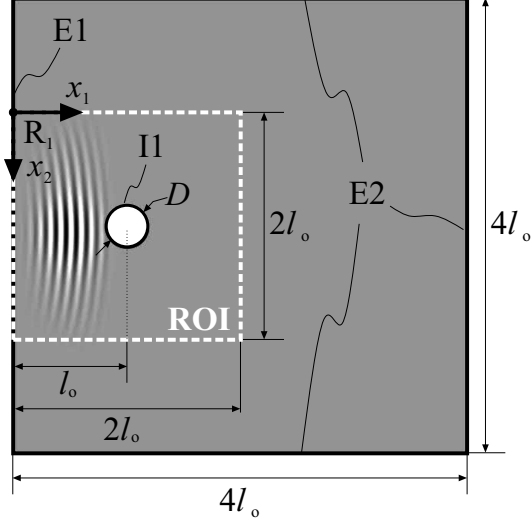


Figure 9: Top side of the prismatic computational domain, defined by two parallel planes at $x_3 = \pm h$ (the top and bottom sides of the plate) and the plane lateral boundaries E1 and E2, with a through-thickness void, defined by the lateral cylindrical boundary I1 (the hole border). The relative position of the ROI and the reference system employed are shown.

Table 1: Models employed to obtain the analytic approximation $\hat{u}_3^{\text{ai}}(\mathbf{x}_h^{\text{E1}}, t)$ to the out-of-plane component of the incident field at the top surface of the plate. The best-fit values of the parameters of the three models are obtained using a least squares procedure over three selected experimental profiles along the x_1 , x_2 and t directions, respectively. The best-fit values $[a_1]$ and $[c_1]$ of the parameters a_1 and c_1 are used to obtain the central Rayleigh wavenumber k_R and the central temporal frequency f_R , respectively.

complex field	amplitude	phase
$\hat{U}_1(x_1) = U_{1m}(x_1) \exp[j\varphi_{1m}(x_1)]$	not used	$a_1x_1 + a_2$
$\hat{U}_t(t) = U_{tm}(t) \exp[j\varphi_{tm}(t)]$	$\sum_{i=1}^2 b_{1i} \exp\left[-\left(\frac{t - b_{2i}}{b_{3i}}\right)^2\right]$	$c_1t + c_2$
$\hat{U}_2(x_2) = U_{2m}(x_2) \exp[j\varphi_{2m}(x_2)]$	$\frac{p_1}{x_2^2 + q_1x_2 + q_2}$	$e_1x_2^2 + e_2x_2 + e_3$

complex field we reconstruct the Cartesian components of the real displacement of the incident field at any point over the whole section of the plate in E1 using the properties of quasi-Rayleigh wavetrains stated in subsection 2.2.

To obtain $\hat{u}_3^{\text{ai}}(\mathbf{x}_h^{\text{E1}}, t)$ in the first stage, on the one hand, we use the part of the temporal record of the out-of-plane displacement at the top surface of the plate in E1 $\hat{u}_3^{\text{e}}(\mathbf{x}_h^{\text{E1}}, t)$ which corresponds to the incident field (see figure 10.a). On the other hand, from the experimental sequence (see f.i. figure 11), we select a particular frame $\hat{u}_3^{\text{e}}(\mathbf{x}_h, \bar{t})$ at reference time instant \bar{t} in which the wavetrain is completely inside the ROI but without interaction with the hole. From the spatial distribution of the amplitude and phase in this particular frame we can assume that the phase and the amplitude of the incident field can be described as a quasi-cylindrical inhomogeneous wave that diverges from a line-source, parallel to the x_3 axis, which intersect the top surface of the plate at point F (see figure 1.b). In this framework, we derive the complex analytic approximation $\hat{u}_3^{\text{ai}}(\mathbf{x}_h^{\text{E1}}, t)$ by following an objective matching procedure in 6 steps [47]: 1) the position $\mathbf{x}_h^{\text{F}} = (x_1^{\text{F}}, x_2^{\text{F}}, h)$ of the virtual source F at the top surface of the plate is obtained as the center of curvature of the wavefronts of the incident field in the selected frame at \bar{t} ; 2) using $\bar{x}_2 = x_2^{\text{F}}$ over this frame we select the complex profile $\hat{u}_3^{\text{e}}(x_1, \bar{x}_2, h, \bar{t})$ and from the best-fit value $[a_1]$ of the slope of a linear fit to its acoustic phase (the phase of the field $\hat{U}_1(x_1)$ in table 1) we estimate the central wavenumber of the train $k_{\text{R}} = [a_1]$; 3) over the temporal record $\hat{u}_3^{\text{e}}(\mathbf{x}_h^{\text{E1}}, t)$ we select a reference point $\bar{\mathbf{Q}}$ with coordinates (\bar{x}_2, \bar{t}) located roughly at the center of the part of the temporal record corresponding to the incident field (figure 10.a), obtaining the profiles $\hat{u}_3^{\text{e}}(\bar{x}_1, \bar{x}_2, h, t)$ and $\hat{u}_3^{\text{e}}(\bar{x}_1, x_2, h, \bar{t})$ which characterize at $\bar{\mathbf{Q}}$ the distribution of the incident field in the t and x_2 directions, respectively; 4) it is assumed that the the out-of-plane component of the incident field at the top surface of the plate at E1 can be factorized as

$$\hat{u}_3^{\text{ai}}(\mathbf{x}_h^{\text{E1}}, t) := \hat{u}_3^{\text{ai}}(0, x_2, h, t) = u_{30} \exp(j\varphi_{30}) \hat{U}_t(t) \hat{U}_2(x_2), \quad (18)$$

where the models for $\hat{U}_t(t)$ and $\hat{U}_2(x_2)$ are congruent with the usual description of the phase of a cylindrical wave in the Fresnel approximation (table 1); 5) the best-fit values of the parameters of these models are found by matching $\hat{U}_t(t)$ to $\hat{u}_3^{\text{e}}(\bar{x}_1, \bar{x}_2, h, t)$ and $\hat{U}_2(x_2)$ to $\hat{u}_3^{\text{e}}(\bar{x}_1, x_2, h, \bar{t})$ using a least squares procedure. In particular, the best-fit value $[c_1]$ (see table 1) divided by 2π gives an estimate of the central temporal frequency f_{R} of the wavetrain, that must be close to the nominal value of the selected excitation

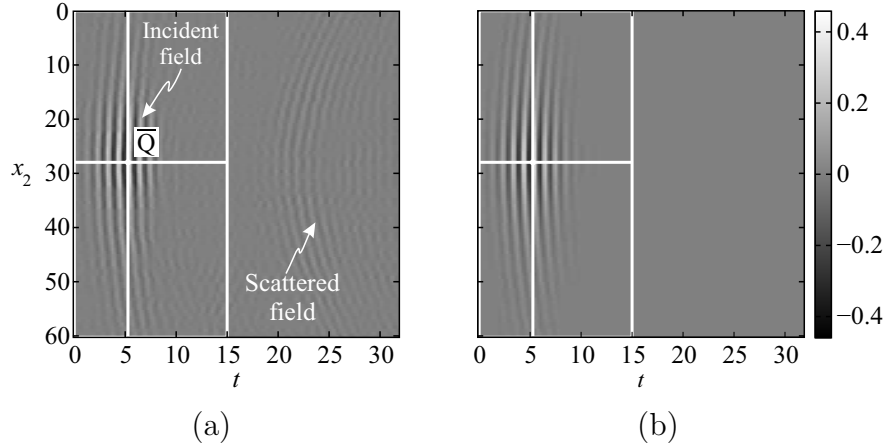


Figure 10: Temporal record of the out-of-plane displacement at boundary E1 ($\mathbf{x}_h^{\text{E1}} = (0, x_2, h)$): (a) experiment $u_3^e(\mathbf{x}_h^{\text{E1}}, t)$, (b) reconstructed incident field employing the analytic approximation $u_3^{\text{ai}}(\mathbf{x}_h^{\text{E1}}, t)$. Point \bar{Q} with coordinates $\bar{x}_2 = 0.028$ mm and $\bar{t} = 5.25$ μs is marked in white. Only the rectangular subzone on the left in (a) has been employed for obtaining the analytic approximation to the non-homogeneous Dirichlet boundary condition in (b). Displacement in units of $\lambda_o/8\pi$. x_2 in millimeters and t in microseconds. The axis numbering corresponds to that of figure 4. Midgray level represents zero.

frequency. From f_R and k_R we obtain the Rayleigh velocity of the plate as $c_R = 2\pi f_R/k_R = [c_1]/[a_1]$ that combined with c_L allows us to determine any other relevant parameter that could be used to characterize the wave propagation in the plate (e.g. the phase velocity of transversal waves c_T , the Poisson's ratio of the plate ν and the associated normalized spectrum of Lamb modes, etc.); 6) u_{30} and φ_{30} are global renormalization factors in amplitude and phase that provide, if necessary, additional degrees of freedom to obtain a better global matching of the analytical approximation considering all the values of the complex amplitude of the incident field within the temporal record $\hat{u}_3^e(\mathbf{x}_h^{\text{E1}}, t)$.

In the second stage we use expression (11) to reconstruct the components of the complex displacement of the incident field at any point over the whole

section of the plate in E1 as

$$\hat{u}_i^{\text{ai}}(\mathbf{x}^{\text{E1}}, t) = \left[\hat{u}_{\parallel f_{\text{Rm}}}^{\text{S0}}(x_3) + \hat{u}_{\parallel f_{\text{Rm}}}^{\text{A0}}(x_3) \right] \times \left[\frac{\mathbf{x}_h^{\text{E1}} - \mathbf{x}_h^{\text{F}}}{|\mathbf{x}_h^{\text{E1}} - \mathbf{x}_h^{\text{F}}|} \cdot \mathbf{a}_i \right] \hat{u}_3^{\text{ai}}(\mathbf{x}_h^{\text{E1}}, t) \quad i = 1, 2 \quad (19\text{a})$$

$$\hat{u}_3^{\text{ai}}(\mathbf{x}^{\text{E1}}, t) = \left[\hat{u}_{\perp f_{\text{Rm}}}^{\text{S0}}(x_3) + \hat{u}_{\perp f_{\text{Rm}}}^{\text{A0}}(x_3) \right] \hat{u}_3^{\text{ai}}(\mathbf{x}_h^{\text{E1}}, t) \quad (19\text{b})$$

from which we derive the analytic approximation to the real displacement incident field as

$$u_i^{\text{ai}}(\mathbf{x}^{\text{E1}}, t) = \text{Re} \left[\hat{u}_i^{\text{ai}}(\mathbf{x}^{\text{E1}}, t) \right] \times E_t(t) E_2(x_2), \quad i = 1, 2, 3 \quad \mathbf{x}^{\text{E1}} \in \text{E1} \quad (20)$$

Auxiliary real envelopes $E_t(t)$ and $E_2(x_2)$ (with pulse profiles with a smooth transition in amplitude from one to zero along t and x_2 , respectively) have been employed in expression (20) to guarantee proper matching of the inhomogeneous boundary condition at E1 with the lateral homogeneous boundary condition at E2 and the zero initial values in the computational domain imposed by expression (17). Practical implementation and processing of numerical data based on this approach has been developed employing self-developed routines in Matlab[®].

4. Results and discussion

We have employed the previously described methodology to analyze the experimental and numerical sequences corresponding to the scattering of quasi-Rayleigh wavetrains by four through-thickness cylindrical holes with nominal diameters 12 mm, 8 mm, 6 mm and 4 mm. After obtaining the experimental sequence for each hole $\hat{u}_3^{\text{e}}(\mathbf{x}_h, t)$ using the procedure described in subsection 3.1, we obtained the analytical approximation to the incident field and the propagation parameters that characterize the wave propagation in the plates using the procedure described in subsection 3.4. We found that the analytical approximation matches the experimental incident field in the corresponding temporal record in all cases, even though pixel to pixel agreement (see figure 10) presents errors at some points in concordance with previously measured noise levels in our case, that are typically around 0.1 of the mean signal level, both in amplitude and phase [47]. In addition, the values of the propagation parameters for each hole and their associated sample averages (table 2) have coherent and reasonable values: on the one hand, the measured

Table 2: Values of the propagation parameters obtained from the coefficients of the analytic approximation $\hat{u}_{3m}^{\text{ai}}(\mathbf{x}_h^{\text{E1}}, t)$ to the out-of-plane component of the incident field at the top surface of the plate. The dispersion around the sample mean is specified after the \pm sign by the rounded-up value of the standard deviation of the mean.

parameter	expression	unit	D/mm				sample mean
			12	8	6	4	
k_R	$[a_1]$	rad/m	2033	2061	2064	2067	2057 ± 8
ω_R	$[c_1]$	(rad/s) 10^6	6.113	6.132	6.165	6.161	6.143 ± 0.002
λ_R	$2\pi/k_R$	mm	3.09	3.05	3.04	3.04	3.05 ± 0.02
f_R	$\omega_R/2\pi$	s 10^6	0.973	0.976	0.981	0.981	0.977 ± 0.002
c_R	$f_R \lambda_R$	m/s	3005	2975	2986	2980	2987 ± 7
c_T	equation (8)	m/s	3227	3191	3204	3197	3205 ± 8
ν	$\frac{(2\chi_{\text{TL}}^2 - 1)}{(2\chi_{\text{TL}}^2 - 2)}$	-	0.327	0.332	0.330	0.331	0.330 ± 0.002
ξ_R	$2hk_R/\pi$	-	6.47	6.56	6.57	6.58	6.55 ± 0.03
γ_R	$4hf_R/c_L$	-	3.059	3.069	3.085	3.083	3.074 ± 0.007

central temporal frequency f_R matches the nominal excitation frequency and the values of the Rayleigh phase velocity, the transversal phase velocity and the Poisson's ratio are within the typical values reported for aluminum; on the other hand, the corresponding normalized values of the frequency and wavenumber of the wavetrains are localized in the qR region of the spectrum (see f.i. the point associated to the averaged normalized frequency $\gamma_R \sim 3.1$ and the associated normalized wavenumber $\xi_R \sim 6.5$ in figure 3). Then, using the analytic approximation and the associated propagation parameters, we solved the IBVP for each hole following the procedure outlined in section 3.2 to obtain the corresponding numerical sequences $\hat{u}_3^n(\mathbf{x}_h, t)$. The typical computational time was of the order of 90 min using a computer with 512 cores for 40000 time-steps of 0.5 ns and a discretization of the computational domain that leads to 5 million of unknowns.

To illustrate the obtained results in the comparison between experimental and numerical data we use representative sequences corresponding to experimental and numerical displacement fields for the cylindrical hole with nominal diameter $D = 12$ mm (figure 11). A visual comparison of the sequences evidences a close agreement in the spatial distribution of the experimental and numerical values of the real displacement. This agreement is confirmed with a more careful visual comparison frame by frame as it is illustrated

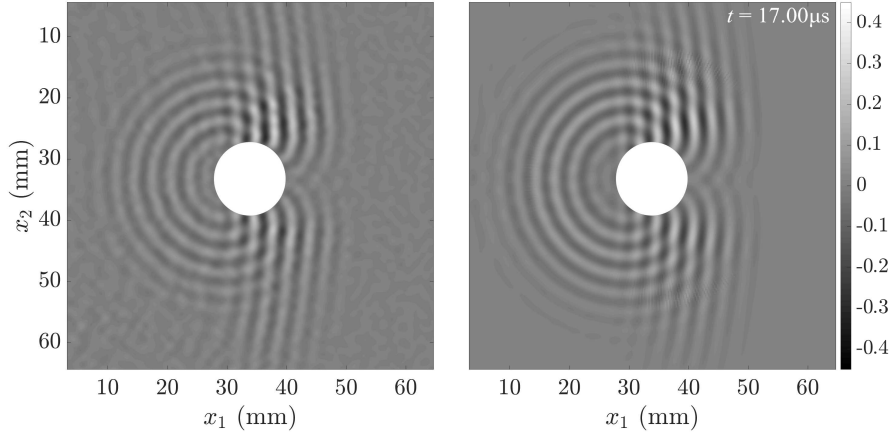


Figure 11: Frame of the video sequence of the out-of-plane displacement field for the scattering of a transient narrow-band quasi-Rayleigh wave by a cylindrical hole with $D = 12$ mm: reference field (experimental) on the left and problem field (numerical) on the right. Amplitude in units of $\lambda_o/8\pi$. Lengths in millimeters. The axis numbering corresponds to that of figure 4. Full sequence in Video 1, MPEG, 1 MB, [video_1_figure_11.mp4].

in figures 12 and 13 where, using a common grey level scale for the images and a common vertical scale for the profiles, the amplitude and phase of the experimental and numerical displacement are presented for two representative instants in the sequences: $t_1 = 8.50 \mu s$ corresponding to the incident field before the interaction with the hole (figure 12), and $t_2 = 17.00 \mu s$ corresponding to the scattered field after the interaction with the hole (figure 13). From these figures, apart from local differences associated to the fluctuations in the experimental field due to presence of speckle, we can conclude that there is a very good matching of the experimental and numerical values. This good matching can be found all along the sequence both for the incident field, which confirms that the employed approach for introducing the incident field using an analytic approximation works properly, and the scattered field, including the forward, lateral and backscattering areas in the image.

This agreement between experiment and numerics found in the visual comparison has been checked over different areas in the image in a more objective quantitative way using the relative rms global errors in L2 norm in

amplitude

$$\varepsilon_{\text{rm}}^{\text{T}} \{R\} (t) := \left[\frac{\sum_{\mathbf{x}_h \in R} |u_{3\text{m}}^{\text{n}}(\mathbf{x}_h, t) - u_{3\text{m}}^{\text{e}}(\mathbf{x}_h, t)|^2}{N_R |u_{3\text{m}}^{\text{ref}}|^2} \right]^{1/2} \quad (21)$$

and in phase

$$\varepsilon_{\text{rM}}^{\text{T}} \{R\} (t) := \left[\frac{\sum_{\mathbf{x}_h \in R} |\varphi_{3\text{M}}^{\text{n}}(\mathbf{x}_h, t) - \varphi_{3\text{M}}^{\text{e}}(\mathbf{x}_h, t)|^2}{N_R |\varphi_{3\text{M}}^{\text{ref}}|^2} \right]^{1/2} \quad (22)$$

being N_R the number of pixels in the selected region R and

$$\begin{aligned} u_{3\text{m}}^{\text{ref}} &= \max [u_{3\text{m}}^{\text{e}}(\mathbf{x}_h, t) \quad \forall (\mathbf{x}_h, t)] \\ \varphi_{3\text{M}}^{\text{ref}} &= \max [\varphi_{3\text{M}}^{\text{e}}(\mathbf{x}_h, t) \quad \forall (\mathbf{x}_h, t)] \end{aligned} \quad (23)$$

the maximum values for amplitude and phase of the field over the ROI in the whole sequence. $\varepsilon_{\text{rm}}^{\text{T}}$ and $\varepsilon_{\text{rM}}^{\text{T}}$ were evaluated for all instants t of the sequence in several sub-zones of interest (see figure 4) and the results (figure 14) show that the value of the relative rms global error is always lower than the typical value 0.1 of the noise-to-signal ratio, in both amplitude and phase, in the experimental PTVH system (which is mainly associated to speckle fluctuations [47]). In other words, a perfect match was obtained—up to a tolerance of the order of the experimental noise. Although this quantitative comparison has been developed only in terms of the acoustic field, it is expected that the agreement between theory and experiment holds for any other relevant quantity of interest that could be derived from the field values (f.i. reflection coefficients, far-field scattering pattern, etc.). Then, the FC(Gram) elastodynamic solver can be considered as a reliable tool for the characterization of the sequences measured with our PTVH system registering the scattering of transient, high-frequency, narrow-band quasi-Rayleigh elastic waves by through-thickness holes.

To illustrate the potential of the FC(Gram) solver for quantitative characterization of temporal and spatial distribution of the acoustic field—f.i in order to optimize the experimental configuration of the PTVH system or the associated data processing and analysis strategy—we present a full 3D sequence for the 12 mm hole that displays the temporal variation of all three components of the displacement vector in the interior volume of the plate (figure 15). In the backscattering area, the incident wave presents the

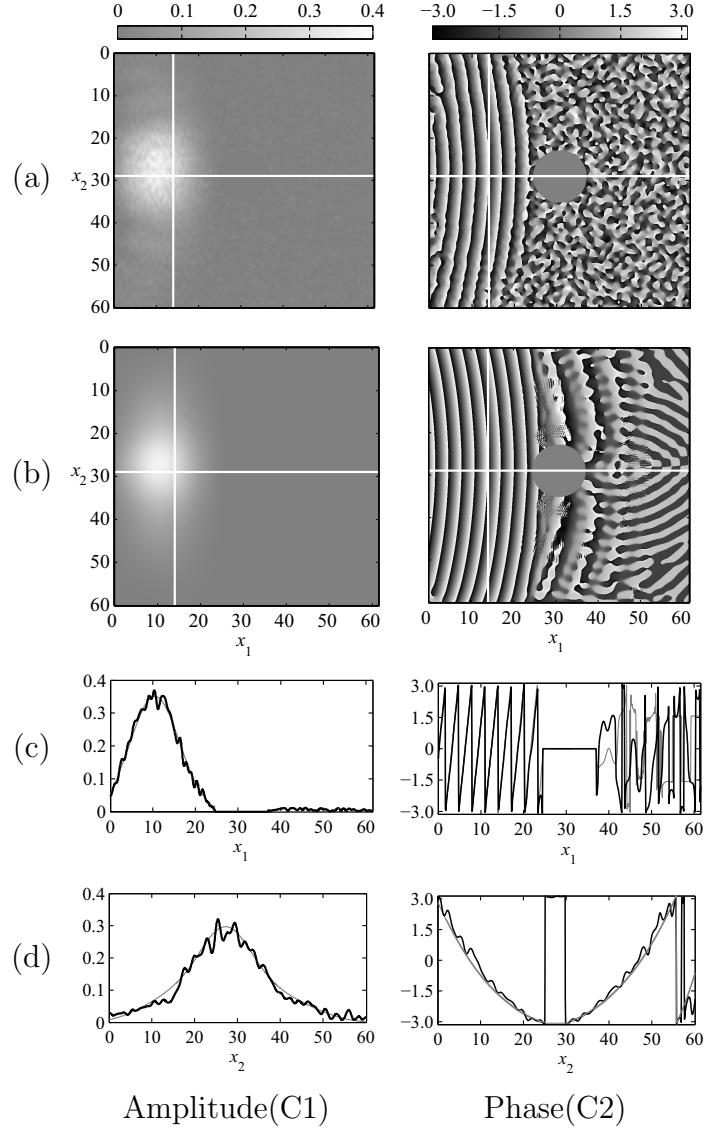


Figure 12: Scattering of a transient narrow-band quasi-Rayleigh wave by a cylindrical hole with $D = 12$ mm at $t_1 = 8.50 \mu\text{s}$: (a) experimental field, (b) numerical field, (c) and (d) profiles along the lines in the x_1 and x_2 directions marked in white in (a) (thick) and (b) (thin). Amplitude in units of $\lambda_o/8\pi$. Phase in radians. Lengths in millimeters. The axis numbering corresponds to that of figure 4.

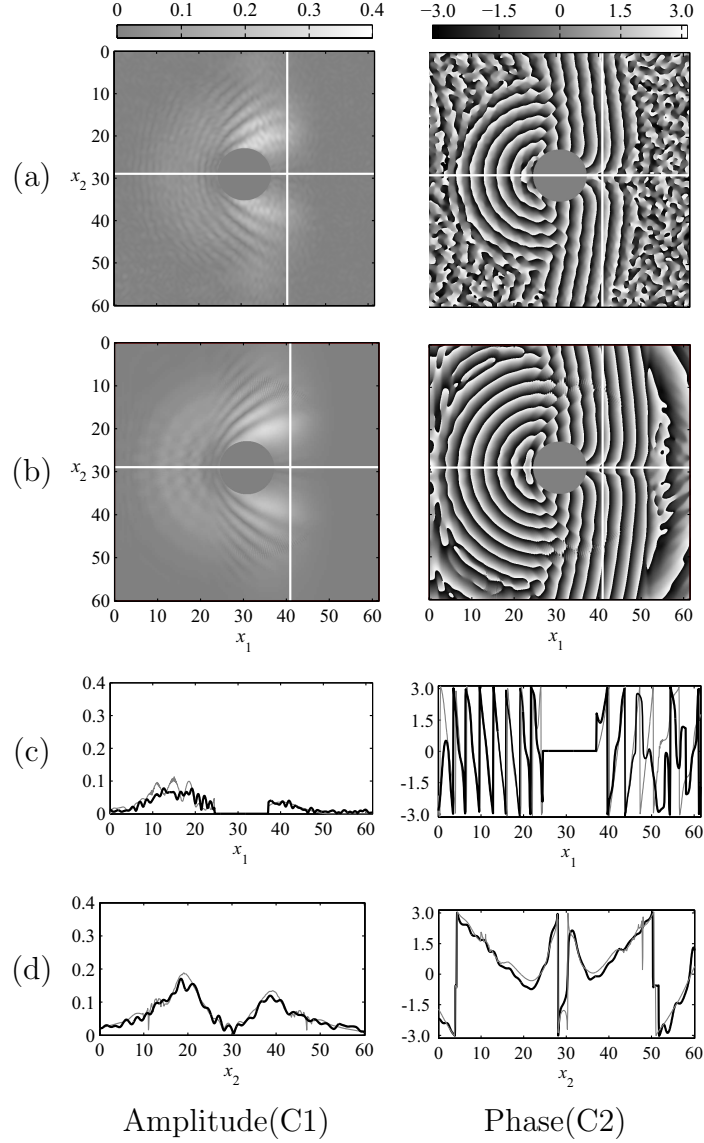


Figure 13: Scattering of a transient narrow-band quasi-Rayleigh wave by a cylindrical hole with $D = 12$ mm at $t_2 = 17.00 \mu\text{s}$: a) experimental field, (b) numerical field, (c) and (d) profiles along the lines in the x_1 and x_2 directions marked in white in (a) (thick) and (b) (thin). Amplitude in units of $\lambda_o/8\pi$. Phase in radians. Lengths in millimeters. The axis numbering corresponds to that of figure 4.

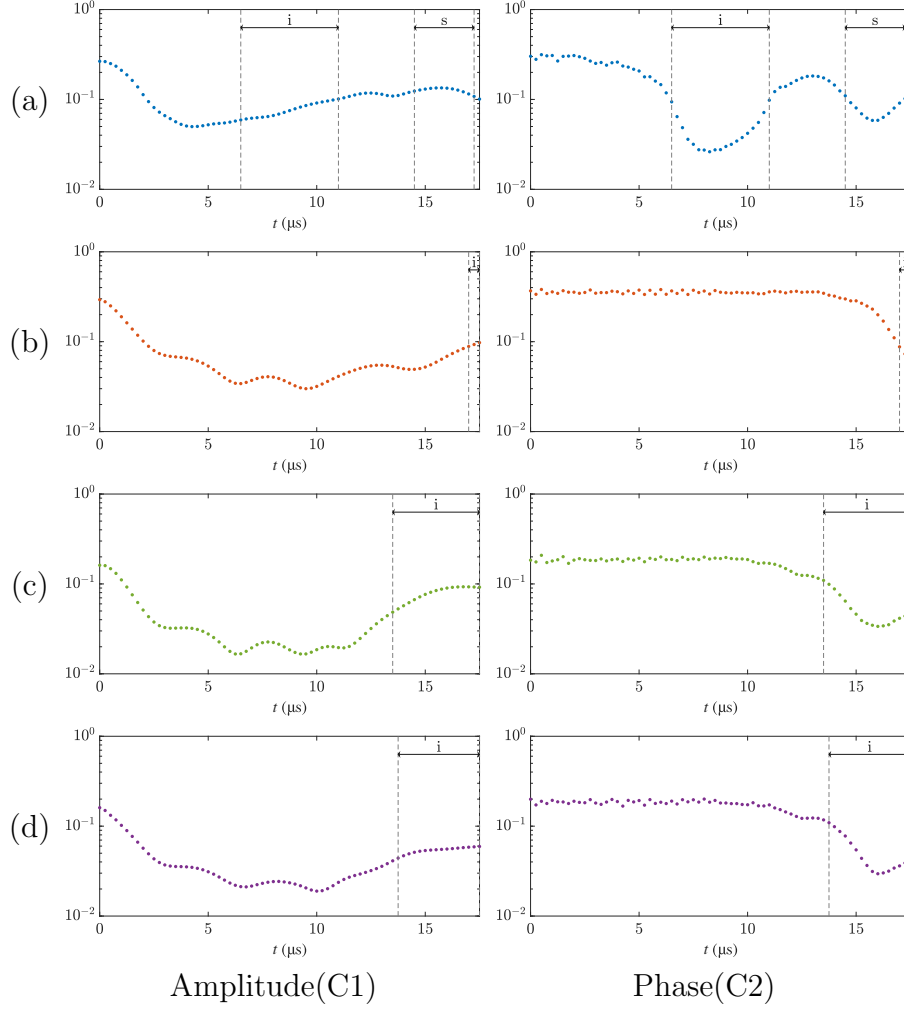


Figure 14: Global relative total error in amplitude $\varepsilon_{\text{rm}}^{\text{T}}(G_{\text{R}})$ and phase $\varepsilon_{\text{rM}}^{\text{T}}(G_{\text{R}})$ between the problem field (numerical) and the reference field (experiment) for the complete sequence of the scattering of a transient narrow-band quasi-Rayleigh wave by cylindrical hole with $D = 12$ mm for several regions G_{R} within the ROI corresponding to those in figure 4: (a) $G_{\text{R}1}$, (b) $G_{\text{R}2}$, (c) $G_{\text{R}3}$ and (d) $G_{\text{R}4}$. The arrows identify the time intervals in which there is an incident (i) or a scattered (s) acoustic field different from zero for each region.

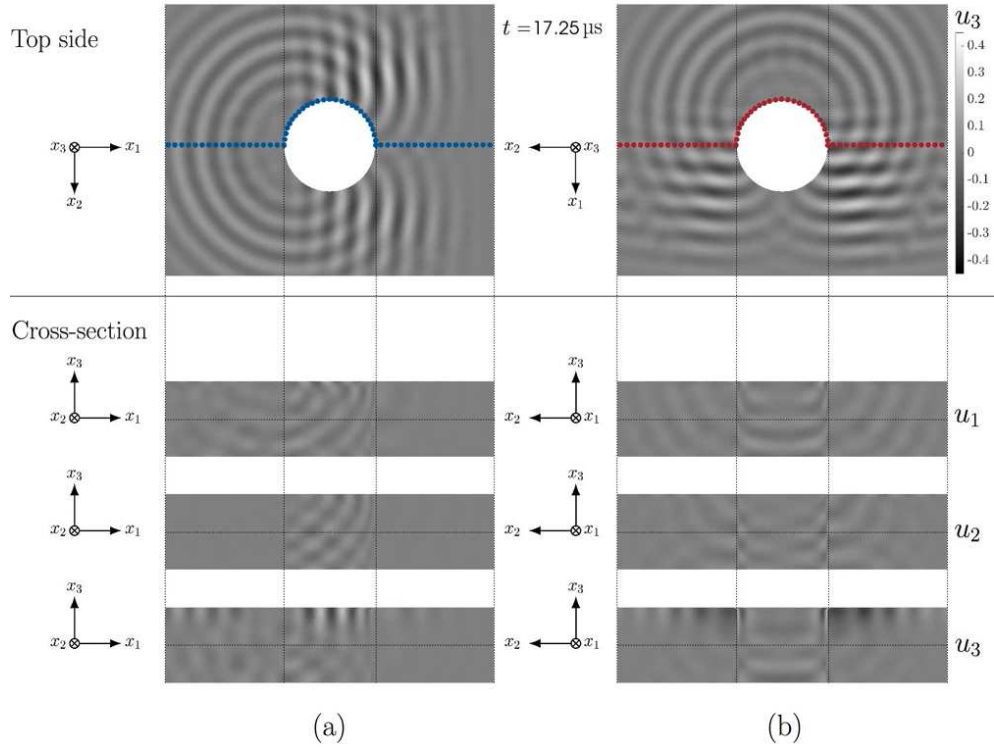


Figure 15: Frame of a video sequence showing the components of the displacement vector in the scattering of a transient narrow-band quasi-Rayleigh wavetrain by a cylindrical hole with $D = 12$ mm: (a) side view from the perspective of the negative x_2 axis, (b) side view from the perspective of the negative x_1 axis. The top side images show the out-of-plane component of the field in a rectangular area of $44 \text{ mm} \times 36 \text{ mm}$, centered at the hole within the ROI in figure 4, and the height of the side view is equal to the plate thickness $2h = 10$ mm. Axes orientation corresponds to those of figures 1 and 4. Amplitude in units of $\lambda_o/8\pi$. Phase in radians. Full sequence in Video 2, MPEG, 2.5MB [video_2_figure_15.mp4].

characteristic spatial distribution of the amplitude of a quasi-Rayleigh wave, with significant values only in a layer of the order of one acoustic wavelength close to the top side of the plate—as clearly visible in the initial frames of the side view of the video corresponding to figure 15.a left. The scattered field, on the other hand, presents well-known features of scattering of elastic waves by defects [56]. Indeed, the reflected wave in the backscattering area is quasi-Rayleigh and it produces a standing wave pattern by interference with the incident field, as can be seen in the late frames of the aforementioned video. Further, the usual modal conversion to SH0 mode [57] is evidenced by the large u_2 displacement that appears in a vicinity of the hole in figure 15 and in the time-interval 11.00 – 19.00 μs in the associated video. The video also displays a wave perturbation that travels downward along the lateral side of the hole, which is subsequently scattered at the bottom, generating an upward perturbation which interferes with the downward perturbation and thus forms a standing wave pattern [58] in the lateral side of the hole (see side view of figure 15.b, center). At the same time, a scattered wave is generated which propagates close to the bottom side of the plate—which can be viewed in the final frames of the side view portions of the video for the u_1 and u_3 components and in figure 15.a left.

5. Conclusions

The scattering of transient narrow-band quasi-Rayleigh waves by through-thickness holes in aluminum plates in the high-frequency regime has been studied. Experimental sequences of scattering patterns measured with a self-developed full-field PTVH system have been compared with the corresponding simulated sequences derived by a state-of-the-art FC(Gram) elastodynamic solver. In addition to a broad agreement in the spatial distribution of the incident and scattered fields for every time instant, which is apparent by visual inspection, a detailed quantitative comparison between experiments and numerics has been presented. Consideration of the relative global errors observed show that a perfect match was obtained, both in amplitude and phase, up to a tolerance of the order of the experimental noise. It is suggested that the combined computation-and-measurement technique bears a significant potential for ultrasonic NDT applications in plate-like structures. Ongoing work focuses on generalization of these techniques to generally-shaped plate-like structures containing complex defects, such as slots, partly through-thickness holes, cracks, etc.

6. Acknowledgments

OB gratefully acknowledges support by NSF and AFOSR and DARPA through contracts DMS-1411876, DMS-1714169, FA9550-15-1-0043 and HR00111720035, and the NSSEFF Vannevar Bush Fellowship under contract number N00014-16-1-2808. The authors from the University of Vigo gratefully acknowledge support by the Spanish *Ministerio de Economía y Competitividad* and the European Commission (ERDF) in the context of the *Plan Nacional de I+D+i* (project number DPI2011-26163), by the *Subdirección Xeral de Promoción Científica e Tecnolóxica universitaria da Xunta de Galicia* in the context of the *Plan Galego de I+D+i* (project number 10PXIB303167PR) and supplementary co-funding from the *Universidade de Vigo* (contract number 09VIA07).

Appendix A. Real and complex description of wave propagation

For any real displacement field $\mathbf{u}(\mathbf{x}, t)$ described by equations (1-2) an associated complex field

$$\hat{\mathbf{u}}(\mathbf{x}, t) = \sum_{i=1}^3 \hat{u}_i(\mathbf{x}, t) \mathbf{a}_i \quad (\text{A.1})$$

with complex components

$$\begin{aligned} \hat{u}_i(\mathbf{x}, t) &= \hat{u}_{im}(\mathbf{x}, t) \exp(-j2\pi ft) \\ &= u_{im}(\mathbf{x}, t) \exp\{j[\varphi_{im}(\mathbf{x}, t) - 2\pi ft]\}, \quad i = 1, 2, 3 \end{aligned} \quad (\text{A.2})$$

can be introduced in such a way that $\mathbf{u}(\mathbf{x}, t) = \text{Re}[\hat{\mathbf{u}}(\mathbf{x}, t)]$ and $u_i(\mathbf{x}, t) = \text{Re}[\hat{u}_i(\mathbf{x}, t)]$, where $\text{Re}[\hat{a}]$ stands for the real part of complex number \hat{a} and j is the imaginary unit. The complex amplitude $\hat{u}_{im}(\mathbf{x}, t)$ of each complex component $\hat{u}_i(\mathbf{x}, t)$ is unambiguously determined by the acoustic amplitude $u_{im}(\mathbf{x}, t)$ and the acoustic phase $\varphi_{im}(\mathbf{x}, t)$ of the corresponding real component $u_i(\mathbf{x}, t)$ and viceversa [59]. Hence, there is a one-to-one correspondence between real and complex components and, as a consequence, between the real displacement field $\mathbf{u}(\mathbf{x}, t)$ and the complex displacement field $\hat{\mathbf{u}}(\mathbf{x}, t)$, which can be also written as $\hat{\mathbf{u}}(\mathbf{x}, t) = \hat{\mathbf{u}}_m(\mathbf{x}, t) \exp(-j2\pi ft)$ where

$$\hat{\mathbf{u}}_m(\mathbf{x}, t) = \sum_{i=1}^3 \hat{u}_{im}(\mathbf{x}, t) \mathbf{a}_i \quad (\text{A.3})$$

is its associated complex amplitude.

Once the complex displacement is well-established, taking as a reference equations (3-4) we can introduce the components of the complex strain tensor $\hat{\epsilon}$ as

$$\hat{\epsilon}_{ij}(\mathbf{x}, t) = \frac{1}{2} \left[\frac{\partial \hat{u}_i(\mathbf{x}, t)}{\partial x_j} + \frac{\partial \hat{u}_j(\mathbf{x}, t)}{\partial x_i} \right], \quad i, j = 1, 2, 3 \quad (\text{A.4})$$

and the complex components of the complex stress tensor $\hat{\tau}$ in the linear elastic regime as

$$\hat{\tau}_{ij}(\mathbf{x}, t) = \lambda_e \delta_{ij} \sum_k \hat{\epsilon}_{kk}(\mathbf{x}, t) + 2\mu_e \hat{\epsilon}_{ij}(\mathbf{x}, t), \quad i, j = 1, 2, 3 \quad (\text{A.5})$$

From the linearity of equations (3-4) and (A.4-A.5) we have that $\epsilon_{ij}(\mathbf{x}, t) = \text{Re}[\hat{\epsilon}_{ij}(\mathbf{x}, t)]$ and $\tau_{ij}(\mathbf{x}, t) = \text{Re}[\hat{\tau}_{ij}(\mathbf{x}, t)]$ and from the linearity of the Lamé-Navier equations (5) we can conclude that the dynamic of the complex displacement field is governed by the complex version of the Lamé-Navier equations

$$\begin{aligned} \frac{(\lambda_e + \mu_e)}{\rho} \sum_{j=1}^3 \frac{\partial^2 \hat{u}_i(\mathbf{x}, t)}{\partial x_i \partial x_j} + \frac{\mu_e}{\rho} \sum_{j=1}^3 \frac{\partial^2 \hat{u}_i(\mathbf{x}, t)}{\partial x_j^2} \\ = \frac{\partial^2 \hat{u}_i(\mathbf{x}, t)}{\partial t^2}, \quad i = 1, 2, 3 \quad \text{in } \Omega \quad (\text{A.6}) \end{aligned}$$

Hence, real and complex fields (with components that have the same acoustic amplitude and the same acoustic phase) provide a completely equivalent description of wave propagation with formally identical real and complex versions of the equations and in such a way that any real field is equal to the real part of the corresponding complex field.

Appendix B. Quasi-Rayleigh waves in plates

Rayleigh waves have significant displacement amplitude only in the vicinity of the plane stress-free surface limiting a homogeneous and isotropic linear elastic semi-infinity solid. Similarly, quasi-Rayleigh waves are a singular case of guided waves in homogeneous and isotropic linear elastic plates, with significant displacement amplitudes only in the vicinity of one of the two plane stress-free surfaces limiting the plate. As quasi-Rayleigh waves results from a particular superposition of Lamb waves, using the same theoretical

framework employed to describe the direct scattering problem in section 2 with the Cartesian reference frame of figure 1, we first consider the case of a plane Lamb wave traveling in the x_1 direction in harmonic regime for a single temporal frequency f . In this conditions it can be shown [49] that wave propagation can be analyzed using plane strain regime ($u_2 = 0$ and $\partial/\partial x_2 = 0$) and that the in-plane (\parallel) and out-of-plane (\perp) components of the displacement are superposition of symmetric and anti-symmetric Lamb modes (i.e. perturbations with displacements that are, respectively, symmetric and anti-symmetric with respect to the mean plane of the plate $x_3 = 0$) with associated complex amplitudes that can be written for the symmetric case as

$$\hat{u}_{\parallel fm}^S(x_3) = j(k_1 B \cos k_{L3} x_3 - k_{T3} C \cos k_{T3} x_3) \quad (\text{B.1a})$$

$$\hat{u}_{\perp fm}^S(x_3) = -k_{L3} B \sin k_{L3} x_3 - k_1 C \sin k_{T3} x_3 \quad (\text{B.1b})$$

and for anti-symmetric case as

$$\hat{u}_{\parallel fm}^A(x_3) = j(k_1 A \sin k_{L3} x_3 + k_{T3} D \sin k_{T3} x_3) \quad (\text{B.2a})$$

$$\hat{u}_{\perp fm}^A(x_3) = k_{L3} A \cos k_{L3} x_3 - k_1 D \cos k_{T3} x_3 \quad (\text{B.2b})$$

being

$$k_{L3}^2 = \frac{\omega^2}{c_L^2} - k_1^2 \quad (\text{B.3a})$$

$$k_{T3}^2 = \frac{\omega^2}{c_T^2} - k_1^2 \quad (\text{B.3b})$$

Each Lamb mode results from the superposition of longitudinal and transversal perturbations with a common effective axial wavenumber k_1 and stationary spatial distribution of the displacement along the x_3 direction characterized by k_{L3} and k_{T3} , respectively. The complex fields for the in-plane and out-of-plane components of each mode can be obtained multiplying the corresponding complex amplitudes, given by expression (B.1-B.2), by the phase factor $\exp[j(k_1 x_1 - 2\pi f t)]$ (although sub-indexes 1 and 3 would be the natural notation for the quantities associated to the two non-zero components of the displacement in this case, sub-indexes \parallel and \perp are more adequate to consider the case of quasi-Rayleigh waves with cylindrical symmetry later on).

Applying the stress-free boundary condition at the surface of the plate for the symmetric case (due to the symmetry it is enough to impose the boundary condition at $x_3 = h$) an homogeneous system of equation for B and C is obtained that has a non trivial solution verifying

$$\frac{B}{C} = \frac{2k_1 k_{T3} \cos k_{T3} h}{(k_1^2 - k_{T3}^2) \cos k_{L3} h} = -\frac{(k_1^2 - k_{T3}^2) \sin k_{T3} h}{2k_1 k_{L3} \sin k_{L3} h} \quad (\text{B.4})$$

if and only if the determinant of the coefficients is zero, which gives the dispersion relation for symmetric Lamb modes

$$(k_1^2 - k_{T3}^2)^2 \cos k_{L3} h \sin k_{T3} h + 4k_{L3} k_{T3} k_1^2 \sin k_{L3} h \cos k_{T3} h = 0 \quad (\text{B.5})$$

Following the same scheme for the anti-symmetric case we obtain that the non trivial solution verifies

$$\frac{A}{D} = -\frac{2k_1 k_{T3} \sin k_{T3} h}{(k_1^2 - k_{T3}^2) \sin k_{L3} h} = \frac{(k_1^2 - k_{T3}^2) \cos k_{T3} h}{2k_1 k_{L3} \cos k_{L3} h} \quad (\text{B.6})$$

provided that the determinant of the coefficients is zero, which gives the dispersion relation for anti-symmetric Lamb modes

$$(k_1^2 - k_{T3}^2)^2 \sin k_{L3} h \cos k_{T3} h + 4k_{L3} k_{T3} k_1^2 \cos k_{L3} h \sin k_{T3} h = 0 \quad (\text{B.7})$$

For each temporal frequency f , an integer finite number of propagating Lamb modes and an infinite number of non-propagating Lamb modes could be excited in the plate at the same time (figure 3). Each propagating Lamb mode (symmetric or anti-symmetric) has a characteristic axial real wavenumber k_1 and travels along direction x_1 (parallel to the center plane of the plate) with a well-defined phase velocity, maintaining its transversal stationary displacement distribution within the plate section during propagation in areas without defects [60]. A non-propagating Lamb mode shares formally the same properties than a propagating one, but has complex axial wavenumber and phase velocity and its amplitude decays to negligible values at distances of the order of a few acoustic wavelengths.

A quasi-Rayleigh plane harmonic guided wave is just the superposition of the plane harmonic waves of a symmetric S0 Lamb mode and an anti-symmetric A0 Lamb mode with the same temporal frequency f within the so-called quasi-Rayleigh range and with the same value of their amplitudes at the top surface of the plate. The S0 and A0 modes are, respectively,

the symmetric and anti-symmetric propagating Lamb modes with the lowest order. They have no cut-off and in the quasi-Rayleigh region of the spectrum at high frequencies (see qR region in figure 3) become non-dispersive and have practically the same propagation wavenumber k_1 and a common phase velocity, which is the Rayleigh phase velocity of the plate c_R . Hence, the complex amplitude of the components of the displacement of the plane harmonic quasi-Rayleigh wave can be written as

$$\hat{u}_{\parallel f_m}(x_3) = [\hat{u}_{\parallel f_m}^{S0}(x_3) + \hat{u}_{\parallel f_m}^{A0}(x_3)] \quad (\text{B.8a})$$

$$\hat{u}_{\perp f_m}(x_3) = [\hat{u}_{\perp f_m}^{S0}(x_3) + \hat{u}_{\perp f_m}^{A0}(x_3)] \quad (\text{B.8b})$$

verifying the condition

$$\frac{\hat{u}_{\parallel f_m}(h)}{2} = \hat{u}_{\parallel f_m}^{S0}(h) = \hat{u}_{\parallel f_m}^{A0}(h) \quad (\text{B.9a})$$

$$\frac{\hat{u}_{\perp f_m}(h)}{2} = \hat{u}_{\perp f_m}^{S0}(h) = \hat{u}_{\perp f_m}^{A0}(h) \quad (\text{B.9b})$$

where $\hat{u}_{\parallel f_m}^{S0}(x_3)$ and $\hat{u}_{\perp f_m}^{S0}(x_3)$ are given by expression (B.1) and $\hat{u}_{\parallel f_m}^{A0}(x_3)$ and $\hat{u}_{\perp f_m}^{A0}(x_3)$ by expression (B.2) in the particular case that modes S0 and A0 have the same value of k_1 and so, share the same values of k_{L3} and k_{T3} , given by equation (B.3) in terms of f , k_1 and the phase velocities of the plate c_L and c_T . Inserting (B.4) and (B.6) with these common values (k_{L3} , k_{T3} and k_1) in expressions (B.1) and (B.2), respectively, and using (B.9) we can obtain the normalized values of the complex amplitude of the in-plane and out-of-plane components of the associated displacement for the S0 and A0 modes with respect to the value of the complex amplitude of out-of-plane component of the quasi-Rayleigh harmonic plane wave at the top surface of

the plate as

$$\begin{aligned}
\hat{u}_{\parallel f_m}^{S0}(x_3) &= \frac{\hat{u}_{\parallel f_m}^{S0}(x_3)}{\hat{u}_{\perp f_m}(h)} \\
&= j \left[(k_1^2 - k_{T3}^2) \cos k_{L3} x_3 \sin k_{T3} h \right. \\
&\quad \left. + 2k_{L3} k_{T3} \sin k_{L3} h \cos k_{T3} x_3 \right] \\
&\quad \times (2\chi_{RT}^2 k_{L3} k_1 \sin k_{L3} h \sin k_{T3} h)^{-1} \tag{B.10a}
\end{aligned}$$

$$\begin{aligned}
\hat{u}_{\perp f_m}^{S0}(x_3) &= \frac{\hat{u}_{\perp f_m}^{S0}(x_3)}{\hat{u}_{\perp f_m}(h)} \\
&= \left[- (k_1^2 - k_{T3}^2) \sin k_{L3} x_3 \sin k_{T3} h \right. \\
&\quad \left. + 2k_1^2 \sin k_{L3} h \sin k_{T3} x_3 \right] \\
&\quad \times (2\chi_{RT}^2 k_1^2 \sin k_{L3} h \sin k_{T3} h)^{-1} \tag{B.10b}
\end{aligned}$$

$$\begin{aligned}
\hat{u}_{\parallel f_m}^{A0}(x_3) &= \frac{\hat{u}_{\parallel f_m}^{A0}(x_3)}{\hat{u}_{\perp f_m}(h)} \\
&= -j \left[(k_1^2 - k_{T3}^2) \sin k_{L3} x_3 \cos k_{T3} h \right. \\
&\quad \left. + 2k_{L3} k_{T3} \cos k_{L3} h \sin k_{T3} x_3 \right] \\
&\quad \times (2\chi_{RT}^2 k_{L3} k_1 \cos k_{L3} h \cos k_{T3} h)^{-1} \tag{B.10c}
\end{aligned}$$

$$\begin{aligned}
\hat{u}_{\perp f_m}^{A0}(x_3) &= \frac{\hat{u}_{\perp f_m}^{A0}(x_3)}{\hat{u}_{\perp f_m}(h)} \\
&= \left[- (k_1^2 - k_{T3}^2) \cos k_{L3} x_3 \cos k_{T3} h \right. \\
&\quad \left. + 2k_1^2 \cos k_{L3} h \cos k_{T3} x_3 \right] \\
&\quad \times (2\chi_{RT}^2 k_1^2 \cos k_{L3} h \cos k_{T3} h)^{-1} \tag{B.10d}
\end{aligned}$$

Once the particular characteristic values of the phase velocities of the plate c_L , c_T and c_R have been established (only two of them are independent as we have pointed out previously) these normalized distributions (figure B.1) are completely determined by specifying, on the one hand, the thickness of the plate $2h$ and, on the other hand, the temporal frequency f or the corresponding axial wavenumber k_1 . Then, using (B.10) in (B.8) results

$$\hat{u}_{\parallel f_m}(x_3) = [\hat{u}_{\parallel f_m}^{S0}(x_3) + \hat{u}_{\parallel f_m}^{A0}(x_3)] \hat{u}_{\perp f_m}(h) \tag{B.11a}$$

$$\hat{u}_{\perp f_m}(x_3) = [\hat{u}_{\perp f_m}^{S0}(x_3) + \hat{u}_{\perp f_m}^{A0}(x_3)] \hat{u}_{\perp f_m}(h) \tag{B.11b}$$

and multiplying both sides by $\exp [j (k_1 x_1 - 2\pi f t)]$ we obtain

$$\hat{u}_{\parallel f}(\mathbf{x}, t) = [\hat{u}_{\parallel f m}^{\text{S0}}(x_3) + \hat{u}_{\parallel f m}^{\text{A0}}(x_3)] \hat{u}_{\perp f}(\mathbf{x}_h, t) \quad (\text{B.12a})$$

$$\hat{u}_{\perp f}(\mathbf{x}, t) = [\hat{u}_{\perp f m}^{\text{S0}}(x_3) + \hat{u}_{\perp f m}^{\text{A0}}(x_{3f})] \hat{u}_{\perp f}(\mathbf{x}_h, t) \quad (\text{B.12b})$$

which allow us to reconstruct the in-plane and out-plane complex component of the quasi-Rayleigh plane harmonic wave inside the plate in terms of its out-of-plane complex component at top surface of the plate and the normalized transversal distributions of S0 and A0 modes given by expression (B.10).

Despite the fact we have considered in the previous analysis the case of a plane harmonic quasi-Rayleigh wave propagation along the x_1 direction, it can be shown that expressions (B.1)-(B.12) are also valid for the case of cylindrical harmonic quasi-Rayleigh wave generated by a line source located in the x_3 axis, provided that we interchange coordinate x_1 by the radial cylindrical coordinate r (i.e. the phase factor $\exp [j (k_1 x_1 - 2\pi f t)]$ by the phase factor $\exp [j (k_1 r - 2\pi f t)]$) and taking into account that in this case the in-plane component is along the radial direction [60]. Hence, using the projection of the radial displacement along the x_1 and x_2 direction we obtain the Cartesian components of the complex displacement of the harmonic quasi-Rayleigh wave with cylindrical symmetry as

$$\begin{aligned} \hat{u}_{if}^i(\mathbf{x}, t) &= [\hat{u}_{\parallel f m}^{\text{S0}}(x_3) + \hat{u}_{\parallel f m}^{\text{A0}}(x_3)] \\ &\quad \times \left[\frac{\mathbf{x}_h}{|\mathbf{x}_h|} \cdot \mathbf{a}_i \right] \hat{u}_{3f}^i(\mathbf{x}_h, t) \quad i = 1, 2 \end{aligned} \quad (\text{B.13a})$$

$$\hat{u}_{3f}^i(\mathbf{x}, t) = [\hat{u}_{\perp f m}^{\text{S0}}(x_3) + \hat{u}_{\perp f m}^{\text{A0}}(x_3)] \hat{u}_{3f}^i(\mathbf{x}_h, t) \quad (\text{B.13b})$$

In the more general case that the line-source is not coincident with the x_3 axis and intersects the top surface of the plate at a virtual point source F with position vector $\mathbf{x}_h^F = (x_1^F, x_2^F, h)$ (see figure 1.b) we have

$$\begin{aligned} \hat{u}_{if}^i(\mathbf{x}, t) &= [\hat{u}_{\parallel f m}^{\text{S0}}(x_3) + \hat{u}_{\parallel f m}^{\text{A0}}(x_3)] \\ &\quad \times \left[\frac{\mathbf{x}_h - \mathbf{x}^F}{|\mathbf{x}_h - \mathbf{x}^F|} \cdot \mathbf{a}_i \right] \hat{u}_{3f}^i(\mathbf{x}_h, t) \quad i = 1, 2 \end{aligned} \quad (\text{B.14a})$$

$$\hat{u}_{3f}^i(\mathbf{x}, t) = [\hat{u}_{\perp f m}^{\text{S0}}(x_3) + \hat{u}_{\perp f m}^{\text{A0}}(x_3)] \hat{u}_{3f}^i(\mathbf{x}_h, t) \quad (\text{B.14b})$$

In the case of a narrow band quasi-Rayleigh wavetrain, as the one described in subsection 2.2, we can assume that the normalized transversal

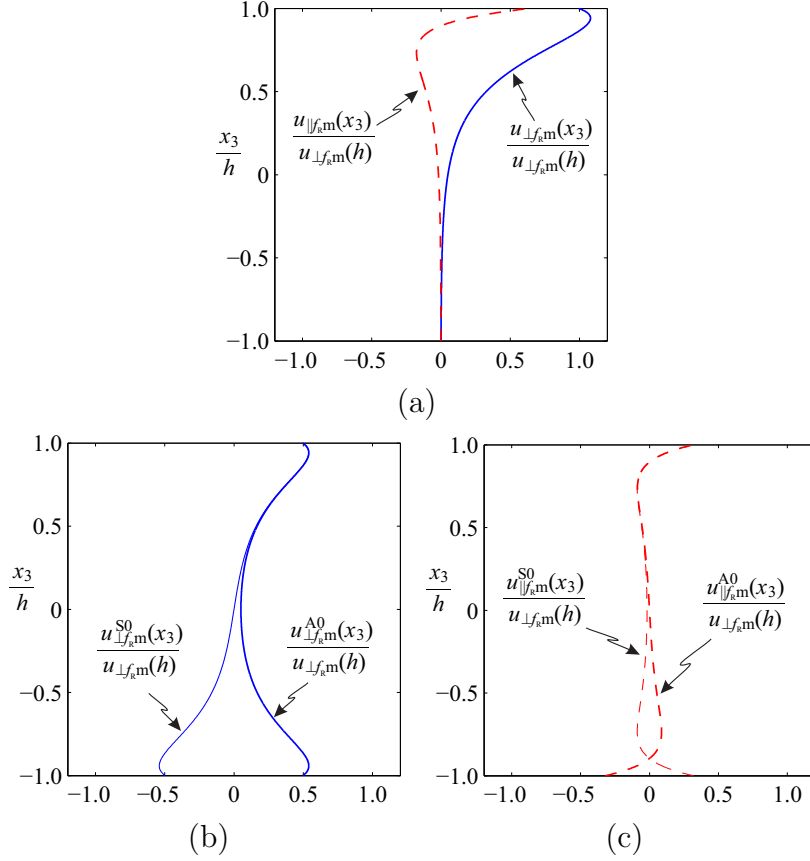


Figure B.1: Plane harmonic quasi-Rayleigh wave traveling in the x_1 direction of a plate with thickness $2h$ for a normalized frequency $\gamma_R = 3.1$ (i.e. close to the situation in our experiments): (a) amplitudes of the in-plane $u_{\parallel f_{\text{Rm}}}(x_3)$ and out-of-plane $u_{\perp f_{\text{Rm}}}(x_3)$ displacements of the quasi-Rayleigh wave, (b) amplitude of the out-of-plane displacements $u_{\perp f_{\text{Rm}}}^{\text{S0}}(x_3)$ and $u_{\perp f_{\text{Rm}}}^{\text{A0}}(x_3)$ of the S0 and A0 components of the quasi-Rayleigh wave, (c) amplitude of the in-plane displacements $u_{\parallel f_{\text{Rm}}}^{\text{S0}}(x_3)$ and $u_{\parallel f_{\text{Rm}}}^{\text{A0}}(x_3)$ of the S0 and A0 components of the quasi-Rayleigh wave. The amplitudes are normalized with respect to the amplitude of the out-of-plane displacement of the quasi-Rayleigh wave at the top surface of the plate $u_{\perp f_{\text{Rm}}}(h)$. The amplitude is positive or negative when is in phase or out of phase by π with respect to $u_{\perp f_{\text{Rm}}}(h)$. The vertical coordinate is normalized with respect to h .

distribution of anyone of its harmonic components is nearly equal to the normalized transversal distribution of the harmonic component with frequency and wavenumber equal to the central frequency f_R and central wavenumber k_R of the train. In this conditions, the complex field of the each harmonic component can be approximated as

$$\hat{u}_{if}^i(\mathbf{x}, t) = [\hat{u}_{\parallel f_{Rm}}^{S0}(x_3) + \hat{u}_{\parallel f_{Rm}}^{A0}(x_3)] \times \left[\frac{\mathbf{x}_h - \mathbf{x}_h^F}{|\mathbf{x}_h - \mathbf{x}_h^F|} \cdot \mathbf{a}_i \right] \hat{u}_{3f}^i(\mathbf{x}_h, t) \quad i = 1, 2 \quad (\text{B.15a})$$

$$\hat{u}_{3f}^i(\mathbf{x}, t) = [\hat{u}_{\perp f_{Rm}}^{S0}(x_3) + \hat{u}_{\perp f_{Rm}}^{A0}(x_3)] \hat{u}_{3f}^i(\mathbf{x}_h, t) \quad (\text{B.15b})$$

Using (B.15) with (9-10) we get expression (11).

References

- [1] J. Fernández, A. Doval, C. Trillo, J. Deán, J. López, Video ultrasonics by pulsed TV holography: A new capability for non-destructive testing of shell structures, *International Journal of Optomechatronics* 1 (2) (2007) 122–153.
- [2] F. Amlani, O. P. Bruno, An fc-based spectral solver for elastodynamic problems in general three-dimensional domains, *Journal of Computational Physics* 307 (2016) 333–354.
- [3] A. Birks, R. Green Jr. (technical eds.), P. McIntire (ed.), *Nondestructive testing handbook*, 2nd Edition, Vol. 7, *Ultrasonic Testing*, American Society for Nondestructive Testing, Columbus, OH, USA, 1991.
- [4] J. Rose, The upcoming revolution in ultrasonic guided waves, in: *Non-destructive Characterization for Composite Materials, Aerospace Engineering, Civil Infrastructure, and Homeland Security*, Vol. Proc. of SPIE Vol. 7983, 2011, pp. 798302–1 to 30.
- [5] M. Mitra, S. Gopalakrishnan, Guided wave based structural health monitoring: A review, *Smart Mater. Struct.* 25 () (2016) 053001–1/27.
- [6] R. Green Jr., Non-contact ultrasonic techniques, *Ultrasonics* 42 () (2004) 9–16.

- [7] M. Castaings, P. Cawley, The generation, propagation, and detection of lamb waves in plates using air-coupled ultrasonic transducers, *Journal of the Acoustical Society of America* 100 (5) (1996) 3070–3077.
- [8] S. Boonsang, R. Dewhurst, Signal enhancement in rayleigh wave interactions using a laser-ultrasound/emat imaging system, *Ultrasonics* 43 (7) (2005) 512–523.
- [9] M. Rosli, R. Edwards, Y. Fan, In-plane and out-of-plane measurements of rayleigh waves using emats for characterising surface cracks, *NDT and Evaluation International* 49 () (2012) 1–9.
- [10] C. Scruby, L. Drain, *Laser Ultrasonics. Techniques and Applications*, Adam Hilger (Bristol), 1990.
- [11] R. Dewhurst, Q. Shan, Optical remote measurement of ultrasound, *Meas. Sci. Technol.* 10 (11) (1999) R139–R168.
- [12] P. Wilcox, Omni-directional guided wave transducer arrays for the rapid inspection of large areas of plate structures, *IEEE Transactions on Ultrasonics, Ferroelectrics, and Frequency Control* 50 (6) (2003) 699–709.
- [13] J. Knuuttila, P. Tikka, M. Salomaa, Scanning michelson interferometer for imaging surface acoustic wave fields, *Optics Letters* 25 (9) (2000) 613–615.
- [14] S. Yashiro, J. Takatsubo, N. Toyama, An ndt technique for composite structures using visualized lamb-wave propagation, *Composites Science and Technology* 67 (15-16) (2007) 3202–3208.
- [15] X. Zhao, R. Royer, S. Owens, J. Rose, Ultrasonic lamb wave tomography in structural health monitoring, *Smart Mater. Struct.* 20 () (2011) 105002–1 to 20.
- [16] K. Nakano, K. Hane, S. Okuma, T. Eguchi, Visualization of 50 mhz surface acoustic wave propagation using stroboscopic phase-shift interferometry, *Optical Review* 4 (2) (1997) 265–269.
- [17] J. Blackshire, B. Duncan, Interferometric and holographic imaging of surface-breaking cracks, *Optical Engineering* 43 (6) (2004) 1366–1374.

- [18] K. Telschow, V. Deason, R. Schley, S. Watson, Direct imaging of traveling lamb waves in plates using photorefractive dynamic holography, *Journal of the Acoustical Society of America* 106 (5) (1999) 2578–2587.
- [19] K. S. Dharmasaktu, A. Kumar, K. Singh, Out-of-plane vibration measurement by speckle photography using photorefractive BaTiO₃ crystal, *Optical Engineering* 40 (6) (2001) 1132–1137.
- [20] B. Bard, G. Gordon, S. Wu, Laser-modulated phase-stepping digital shearography for quantitative full-field imaging of ultrasonic waves, *Journal of the Acoustical Society of America* 103 (6) (1998) 3327–3335.
- [21] C. Trillo, D. Cernadas, A. Doval, C. López, B. Dorrío, J. Fernández, Detection of transient surface acoustic waves of nanometric amplitude with double-pulsed TV holography, *Applied Optics* 42 (7) (2003) 1228–1235.
- [22] C. Trillo, A. Doval, D. Cernadas, O. López, J. López, B. Dorrío, J. Fernández, M. Pérez-Amor, Measurement of the complex amplitude of transient surface acoustic waves using double-pulsed TV holography and a two-stage spatial Fourier transform method, *Measurement Science & Technology* 14 (12) (2003) 2127–2134.
- [23] D. Cernadas, C. Trillo, A. Doval, O. López, C. López, B. Dorrío, J. Fernández, M. Pérez Amor, Non-destructive testing of plates based on the visualisation of lamb waves by double pulsed tv holography, *Mechanical Systems and Signal Processing* 20 () (2006) 1338–1349.
- [24] P. Bettess, Short-wave scattering: Problems and techniques, *Phil. Trans. R. Soc. Lond. A* 362 (1816) (2004) 421–443.
- [25] W. Ostachowicz, M. Radzieski, P. Kudela, Comparison studies of full wavefield signal processing for crack detection, *Strain* 50 () (2014) 275–291.
- [26] L. Bond, Numerical techniques and their use to study wave propagation and scattering - a review, in: Y. R. S.K. Datta, J.D. Achenbach (Ed.), *Elastic waves and ultrasonic nondestructive evaluation*, Elsevier Science Publisher, 1990, pp. 17–27.

- [27] T. Grahn, Lamb wave scattering from a circular partly through-thickness hole in a plate, *Wave Motion* 37 () (2003) 63–80.
- [28] B. Masserey, P. Fromme, Analysis of high frequency guided wave scattering at a fastener hole with a view to fatigue crack detection, *Ultrasonics* 76 () (2017) 78–86.
- [29] C. Travaglini, C. Bescond, M. Viens, P. Belanger, Feasibility of high frequency guided wave crack monitoring, *Structural Health Monitoring* 16 (4) (2017) 418–427.
- [30] Y. Cho, J. Rose, A boundary element solution for a mode conversion study on the edge reflection of lamb waves, *J. Acoust. Soc. Am.* 99 (4 I) (1996) 2097–2109.
- [31] S. Banerjee, T. Kundu, Scattering of ultrasonic waves by internal anomalies in plates, *Optical Engineering* 46 (5) (2007) 053601–1 to –9.
- [32] P. Paćko, T. Bielak, A. Spencer, W. Staszewski, T. Uhl, K. Worden, Lamb wave propagation modelling and simulation using parallel processing architecture and graphical cards, *Smart Mater. Struct.* 21 () (2012) 07500–1/13.
- [33] G. Liu, A combined finite element/strip element method for analyzing elastic wave scattering by cracks and inclusions in laminates, *Computational Mechanics* 28 (1) (2001) 76–81.
- [34] N. Terrien, D. Osmont, D. Royer, F. Lepoutre, A. Déom, A combined finite element and modal decomposition method, *Ultrasonics* 46 () (2007) 74–88.
- [35] C. Vemula, A. Norris, Flexural wave propagation and scattering on thin plates using mindlin theory, *Wave Motion* 26 (1) (1997) 1–12.
- [36] C. Wang, F.-K. Chang, Scattering of plate waves by a cylindrical inhomogeneity, *Journal of Sound and Vibration* 282 (1-2) (2005) 429–451.
- [37] T. Mast, G. Gordon, Quantitative flaw reconstruction from ultrasonic surface wavefields measured by electronic speckle pattern interferometry, *IEEE transactions on ultrasonics, ferroelectrics, and frequency control* 48 (2) (2001) 432–444.

- [38] P. Fromme, M. Sayir, Measurement of the scattering of a Lamb wave by a through hole in a plate, *Journal of the Acoustical Society of America* 111 (3) (2002) 1165–1170.
- [39] J. López-Vázquez, X. Deán-Ben, C. Trillo, A. Doval, J. Fernández, F. Amlani, O. Bruno, Numerical modeling and measurement by pulsed television holography of ultrasonic displacement maps in plates with through-thickness defects, *Optical Engineering* 49 (9) (2010) 095802–1/10.
- [40] P. Rodríguez-Gómez, J. López-Vázquez, C. Trillo, A. Doval, J. Fernández, Transient elastic wave propagation and scattering in plates: comparison between pulsed tv-holography measurements and finite element method predictions, *Optical Engineering* 52 (10) (2013) 101911/1–13.
- [41] O. P. Bruno, M. Lyon, High-order unconditionally stable fc-ad solvers for general smooth domains i. basic elements, *Journal of Computational Physics* 229 (6) (2010) 2009–2033.
- [42] N. Albin, O. P. Bruno, A spectral fc solver for the compressible navier–stokes equations in general domains i: Explicit time-stepping, *Journal of Computational Physics* 230 (16) (2011) 6248–6270.
- [43] N. Albin, O. P. Bruno, T. Y. Cheung, R. O. Cleveland, Fourier continuation methods for high-fidelity simulation of nonlinear acoustic beams, *The Journal of the Acoustical Society of America* 132 (4) (2012) 2371–2387.
- [44] J. P. Boyd, *Chebyshev and Fourier spectral methods*, Courier Corporation, 2001.
- [45] W. D. Henshaw, D. W. Schwendeman, Parallel computation of three-dimensional flows using overlapping grids with adaptive mesh refinement, *Journal of Computational Physics* 227 (16) (2008) 7469–7502.
- [46] C. Trillo, A. Doval, Spatiotemporal Fourier transform method for the measurement of narrowband ultrasonic surface acoustic waves with TV holography, in: *Proceedings of SPIE*, Vol. 6341, 2006, p. 63410M.

- [47] P. Rodríguez-Gómez, Exploración de técnicas de caracterización cuantitativa de defectos en placas metálicas a partir de campos ultrasónicos transitorios bidimensionales detectados mediante holografía-tv, Ph.D. thesis, Universidade de Vigo, PhD Disertation available at <http://hdl.handle.net/11093/910> (2015).
- [48] J. Rose, *Ultrasonic Waves in Solid Media*, Cambridge University Press, Cambridge, 1999, pp. 200–240.
- [49] K. Graff, *Wave motion in elastic Solids*, Dover, 1975.
- [50] A. Doval, A systematic approach to TV-holography, *Measurement Science and Technology* 11 (1) (2000) R1–R36.
- [51] M. . Gockenbach, *Partial Differential Equations: Analytical and Numerical Methods*, Second Edition, Society for Industrial and Applied Mathematics (SIAM, 3600 Market Street, Floor 6, Philadelphia, PA 19104), 2010.
URL <http://books.google.com/books?id=hn1bz4iPmD4C>
- [52] O. P. Bruno, Y. Han, M. M. Pohlman, Accurate, high-order representation of complex three-dimensional surfaces via Fourier continuation analysis, *J. Comput. Phys.* 0021-9991 227 (2) (2007) 1094–1125.
- [53] J. P. Boyd, J. R. Ong, Exponentially-convergent strategies for defeating the Runge phenomenon for the approximation of non-periodic functions, part i: single-interval schemes, *Commun. Comput. Phys.* 5 ((2-4)) (2009).
- [54] O. P. Bruno, Fast, high-order, high-frequency integral methods for computational acoustics and electromagnetics, *Topics in Computational Wave Propagation Direct and Inverse Problems Series, Lecture Notes in Computational Science and Engineering* 31 (2003).
- [55] M. Lyon, O. P. Bruno, High-order unconditionally stable FC-AD solvers for general smooth domains ii. elliptic, parabolic and hyperbolic PDEs; theoretical considerations, *J. Comput. Phys.* 229 (9) (2010) 3358–3381.
doi:10.1016/j.jcp.2010.01.006.
URL <http://dx.doi.org/10.1016/j.jcp.2010.01.006>

- [56] X. Jian, X. Fan, R. Edwards, S. Dixon, Surface-breaking cracks gauging with the use of laser-generated rayleigh waves, *Journal of Applied Physics* 100 () (2006) 064907/1–6.
- [57] O. Diligent, T. Grahn, A. Bostrom, P. Cawley, M. Lowe, The low-frequency reflection and scattering of the S0 Lamb mode from a circular through-thickness hole in a plate: Finite Element, analytical and experimental studies, *J. Acoust. Soc. Am.* 112 (6) (2002) 2589–2601.
- [58] B. Masserey, P. Fromme, On the reflection of coupled rayleigh-like waves at surface defects in plates, *Journal of the Acoustical Society of America* 123 (1) (2008) 88–98.
- [59] M. Born, E. Wolf, *Principles of Optics*, 5th Edition, Pergamon Press, Oxford, 1975.
- [60] J. Achenbach, *Reciprocity in elastodynamics*, Cambridge University Press, Cambridge, 2003, pp. 116–131.